Study of the phase dynamics in moderately damped Josephson junctions and its applications

By

Suman Dhamala

Submitted to the graduate degree program in the Department of Physics and Astronomy and the Graduate Faculty of the University of Kansas
in partial fulfillment of the requirements for the degree of
Doctor of Philosophy

Committee members

Prof. Siyuan Han, Chairperson

Prof. Judy Wu

Prof. Hui Zhao

Prof. Philip Beringer

Prof. Rongqing Hui

Date defended: April 29, 2021

The Dissertation Committee for Suman Dhamala certifies
that this is the approved version of the following dissertation :

Study of the phase dynamics in moderately damped Josephson junctions and its applications

Prof. Siyuan Han, Chairperson

Date approved: May 12, 2021

Abstract

The observation of macroscopic quantum tunneling (MQT) manifests the quantumness of macroscopic variables, such as the phase difference across a Josephson junction (JJ). Since then, MQT has become a hallmark experiment to show the quantum nature of JJ-based devices. It has also paved a way to test other macroscopic quantum effects and has led to engineering a variety of artificial atoms, i.e., qubits. However, in the progress of quantum circuits for different applications, it is crucial to understand the influence of thermal and quantum fluctuations, dissipation, and noise to various quantum devices. Thus, the role of the factors mentioned above and the junction parameters E_J (Josephson coupling energy) and E_C (charging energy) can be scrutinized by understanding the dynamics of the fictitious phase particle. Similarly, in the application perspective, Szilard engine based on SET device are too slow to convert heat into work and are not efficient in-terms of power performance. To overcome the drawbacks, we proposed a high-efficiency fast Szilard engine based on a flux logic device (FLD) and investigated its property numerically and optimize its performance.

In the first part of the dissertation, we studied the phase dynamics of moderately damped Josephson junctions. The time of flight technique is used to measure the switching current distributions (SCDs). Different dynamical states, thermal activation (TA), MQT, and phase diffusion (PD) are identified from SCDs through well-defined criteria. We observed unambiguous evidence of MQT when temperature is below $\sim$ 0.5-0.8 K. The importance of the tilt in the phase dynamics of the junctions, which has been overlooked in previous studies, is clarified. We found that the junction with

larger E_J but the same ω_{p0} requires greater tilt and lower temperature to enter MQT regime.

In the second part of the dissertation, to overcome the limitation of the SET based Szilard engine, we used superconducting quantum interference device (SQUID) as a one-bit flux logic cell to realize a fast Szilard engine for optimal power. In the past decade, due to technological advancement, the study of energy fluctuations in nano-scale systems such as optical or electrical traps and single-electron tunneling (SET) devices has transformed Szilard's engine to experimental realizations. However, the heat engine realized are slow to convert heat into work limiting their performance in speed and power. The SQUID-based flux logic device (FLD) has a high characteristic frequency, $\omega_{\rm p}/2\pi \sim 10^{10}$ Hz, making it an excellent candidate for realizing a high-efficiency Szilard engine with unprecedented performance. We showed that, on average, the proposed heat engine can extract $k_B T \ln 2$ of heat per cycle from the thermal reservoir in the quasi-static (QS) limit. In addition, we showed that the FLD-based Szilard engine delivers maximum power when operated about 200 times faster than the threshold speed of quasi-static operation. Our result demonstrates that Szilard's engine's performance based on FLD exceeds other nano-device implementations by orders of magnitude.

To my wonderful family

Acknowledgements

I have met many supportive people at the University of Kansas (KU) during my Ph.D. journey, and I could not remain at peace without acknowledging them.

First of all, I am grateful to Prof. Siyuan Han, willing to advise me. I was the only student under his supervision during this timeframe. His door was always open to provide insight into a subject matter, and he frequently visited the lab to assist me in my difficulties. I highly appreciate his constant support in shaping me as an experimental physicist and the trust he put in me. It takes a lot of time and effort to master the technique related to low-temperature physics. The wet dilution refrigerator requires a rigorous operation procedure for proper operation. A solid plan to execute an experiment is always required beforehand; else will be the loss of liquid helium, which is costly. The shortage of liquid helium was a problem we faced multiple times to complete our experiment. The simultaneous process of running experiments, collecting data, and analyzing them to get meaningful results within the timeframe by a single person was a pain in the neck. Nevertheless, my supervisor's constant support and interest in the field always encouraged me to move forward, and here I am today, completing the dissertation. Once again, I would like to thank Prof. Han for his guidance and patience in nourishing me as an experimental quantum physicist.

I want to acknowledge our collaborator, Dr. Hao Li, from the University of California Riverside. He fabricated the Y-Ba-Cu-O planar Josephson junctions and provided me an opportunity to characterize them. We had many fruitful scientific discussions, and the results presented in this dissertation would not be possible without his permanent help and support. Also, I would like to acknowledge Dr. Gang Li for providing the flux logic device for Szilard's engine project.

I am thankful to Prof. Judy Wu, Prof. Hui Zhao, Prof. Philip Beringer, and Prof. Rongqing Hui for being part of my thesis committee and their careful evaluation and input to complete the dissertation. Special thanks go to my fellow Ph.D. colleague Peymon Jeresky and Victor Ogungimi. They have constantly helped me to lift the dilution refrigerator insert to change the samples.

I am greatly indebted to the whole physics department for their cooperation in ending this dissertation. To be more specific, I want to thank Kristin for her constant support and handling of queries regarding the financial part, while Joel was always smiling to handle graduate students' problems. Joel is comparable to the health care frontline worker defeating the COVID-19 crisis. I am particularly grateful to our machine shop technicians, Hase Allen and Mark Stockham, for helping to design and make PPMS probes and sample holders. Also, the IT service group led by John Clune and Jason Johnson helped me a lot on setting and resolving the issue related to IT consistently.

Lastly, I want to express the most profound thankfulness to my parents, who always unconditionally supported my life path. My highest gratitude goes to my spouse Nabina Acharya, and her permanent support was praiseworthy.

List of Symbols and Abbreviations

c	Speed of light
e	Elementary charge
k_B	Boltzmann's constant
T	Temperature
$\hbar$	Reduced Planck's constant
ρ	Resistivity
μ_0	Permeability
Φ_0	Magnetic flux quantum ($= h/2e$)
T_c	Critical temperature
m_s	Mass of superconducting electron
n_s	Density of superconducting electrons
φ	Phase
Δ	Superconducting energy gap
λ_L	London penetration depth
ξ	Coherence length
H_c	Critical magnetic field
H_{c1}	Lower critical field
H_{c2}	Upper critical field
$\Psi(\mathbf{r})$	Macroscopic order parameter (wave function)
M	Isotopic mass
ω_D	Debye frequency
ν	Microwave frequency
$\mathbf{B}$	Magnetic field
$\mathbf{E}$	Electric field
$\mathbf{P}$	Total Momentum

$\mathbf{A}$	Vector potential
$\mathbf{J_s}$	Supercurrent density
E_J	Maximum Josephson coupling energy ($= I_c\Phi_0/2\pi$)
E_C	Coulomb charging energy ($= e^2/2C$)
I_c	Critical current
I_s	Junction switching current
I_r	Retrapping current
L_J	Josephson inductance
C	Junction capacitance
R	Resistance
β_C	Stewart Macumber parameter
Q_0	Quality factor ($= \omega_{p0}RC$)
G	Dimensionless damping coefficient ($= 1/Q_0$)
i	Normalized bias current ($= I/I_c$)
$U(\varphi)$	Potential energy of the Josephson junction
ΔU	Potential barrier height
ω_{p0}	Plasma frequency at zero bias ($= \sqrt{2\pi I_C/\Phi_0 C}$)
a_t	Dimensionless thermal damping dependent factor
a_q	Dimensionless quantum damping dependent factor
T_{cr}	TA-to-MQT crossover temperature
Γ	Escape rate
$\langle I_\mathrm{s} \rangle$	Mean switching current
σ	Standard deviation of the switching current distribution
μ_3	Third moment of the switching current distribution
γ_3	Skewness of the switching current distribution ($= \mu_3/\sigma^3$)
L	Superconducting loop inductance
β_L	Potential-shape parameter of SQUID ($= L/L_J = 2\pi L I_c/\Phi_0$)

Φ	Total magnetic flux in SQUID based flux logic device loop
Φ_x	Tilt-tuning flux bias
ε	Energy bias of the double-well potential
ΔU_0	Potential barrier height at $\Phi_x = \Phi_0/2$
Γ_0	Thermal escape rate at $\Phi_x = \Phi_0/2$
t_{D}	Slow drive time
t_{M}	Measurement time
t_{F}	Fast drive time
t_{cycle}	Szilard engine's cycle time ($= t_{\mathrm{D}} + t_{\mathrm{M}} + t_{\mathrm{F}}$)
$\langle Q \rangle$	Average heat absorbed by the Szilard engine
$\langle W \rangle$	Average work done by the Szilard engine
S_{H}	Shannon entropy
F_i	Flux logic device state ($= \pm 1$)
P	Average normalized power output by the Szilard engine
$\Gamma_0 t_{\mathrm{cycle}}$	Normalized Szilard engine cycle time
GL	Ginzburg-Landau
BCS	Bardeen-Cooper-Schrieffer
JJ	Josephson junction
IJJ	Intrinsic Josephson junction
LTS	Low temperature superconductor
HTS	High temperature superconductor
FHIB	Focused Helium Ion Beam
SCD	Switching current distribution
TA	Thermal Activation
MQT	Macroscopic quantum tunneling
PD	Phase diffusion
QPD	Quantum phase diffusion

SQUID	Superconducting Quantum Interference Device
RSFQ	Rapid single flux quantum
MQP	Macroscopic quantum phenomena
ELQ	Energy level quantization
SET	Single electron transistor
STM	Scanning tunneling microscope
S-I-S	Superconductor-Insulator-Superconductor
GB	Grain Boundary
RCSJ	Resistively and capacitively shunted junction
QS	Quasi-static
FLD	Flux logic device

Contents

List of Tables

List of Figures

Chapter 1

Introduction

This chapter aims to build a theoretical framework needed behind the experimental results presented in this dissertation.

1.1 Superconductivity

In 1911, Heike Kamerlingh Onnes discovered that the resistivity, ρ of mercury, drops suddenly to zero when cooled below a specific temperature. He observed that above this specific temperature a.k.a. critical temperature T_c, ρ varies linearly, but when $T \leq T_c = 4.2$ K, ρ drops sharply to zero [1, 2]. This finding leads to the discovery of a new family of conductors named superconductors, for which $\rho = 0$ when cooled below T_c (which is the characteristic of the material). Thus, perfect conductivity becomes the first hallmark property of superconductivity. This experimental finding provided a clear picture that a phase transition from a normal metal state to a superconducting state exists. The exponential rise in heat capacity near T_c and the transition being continuous indicated the phase transition without a latent heat. Besides the abnormal specific heat capacity, there are several other peculiar macroscopic properties of the superconductor, such as the Meissner effect (expulsion of the magnetic field from the interior of the superconductor), and the Isotope

effect (dependence of T_c on the isotopic mass) [3]. The zero resistivity of such materials pointed towards the direction of several exciting applications such as lossless transmission cables, the production of high-power electromagnets, and even energy storage devices. Besides, the discovery of the Josephson effect in 1962 opened up the exciting potential for the use of superconductors in metrology such as voltage standard, ultra sensitive magnetometer (SQUID), and high-speed digital electronic circuits (RSFQ) [4–8].

1.1.1 Phenomenological theory of Superconductivity

H. London developed a linear electrodynamical response theory of the superconductivity [9, 10]. The London equations successfully explained the two hallmark properties of superconductors: perfect conductivity and perfect diamagnetism (Meissner effect). London's equations are based on the two-fluid model (proposed by Gorter and Casimir, 1934), a simple yet useful model for a superconductor's behavior at finite temperature. The model assumes that the superconducting electrons are grouped together and localized in space such that the mean momentum (kinetic plus the field momentum) of the superconducting electrons is zero, i.e. $\langle \mathbf{P} \rangle = m_s \mathbf{v_s} + e_s \mathbf{A}/c = 0$ [1]. The assumption leads to the direct relation between the supercurrent density ($\mathbf{J_s}$) and the vector potential $\mathbf{A}$ of the local magnetic field as

$$\mathbf{J_s} = n_s e_s \langle \mathbf{v_s} \rangle = -\frac{n_s e_s^2 \mathbf{A}}{m_s c}, \tag{1.1}$$

where n_s is the superconducting electron density, m_s is the mass of the super-electron carrying the charge e_s and c is the speed of light. Take the time derivative and the curl on both side of the Eq. (1.1) yields the simplified form of the London's equation (1.2a) and (1.2b). Eqs. (1.2a) and (1.2b) provide a macroscopic electrodynamic behavior of superconductors [11]. They relate the

local electric (**E**) and magnetic (**B**) fields to the supercurrent density ($\mathbf{J_s}$) as

$$\mathbf{E} = \mu_0 \lambda_L^2 \frac{\partial(\mathbf{J_s})}{\partial t} \tag{1.2a}$$

$$\mathbf{B} = -\mu_0 \lambda_L^2 \nabla \times (\mathbf{J_s}), \tag{1.2b}$$

where $\lambda_L = \sqrt{m_s/\mu_0 n_s e_s^2}$ is a material-dependent phenomenological constant known as the Londons penetration depth. The first London equation expresses perfect conductivity in that the electric field accelerates the super-electrons whereas the second equation describes the Meissner effect. The exponential decaying of the magnetic field inside the superconductor is obtained by taking the curl of the Maxwell's relation, $\nabla \times \mathbf{B} = \mu_0 \mathbf{J_s}$ and inserting the value into Eq. (1.2b) , which leads to $\nabla^2 \mathbf{B} = \mathbf{B}/\lambda_L^2$. The general solution for a semi-infinite superconductor is $\mathbf{B} = B_0 \exp(-x/\lambda_L)$ where x is the distance from the surface of the bulk superconductor. It shows that magnetic field penetrates into the superconductor a distance, λ_L [12].

The Ginzburg-Landau (GL) theory (1950) is a modification to London's theory based on Landau's mean-field theory of second-order phase transition [9]. They realized that superconductivity is a quantum phenomenon in which all the superconducting electrons (superfluid) reside in the "macroscopic quantum ground state" described by a macroscopic complex order parameter (wave function) by

$$\Psi(\mathbf{r}) = \sqrt{n_s(\mathbf{r})}\, \mathrm{e}^{i\varphi(\mathbf{r})}, \tag{1.3}$$

where φ is the phase of the order parameter [13]. The superconducting current density is related to the order parameter as

$$\mathbf{J_s} = -\left(\frac{e_s \hbar n_s}{2m_s}\right) \nabla\varphi - \left(\frac{n_s e_s^2}{m_s c}\right) \mathbf{A}. \tag{1.4}$$

We can obtain the second London equation if there is no spacial dependent order parameter. Beyond the results obtained from the London equations, the GL theory predicted a second characteristic length scale ξ, over which spatial changes in Ψ occur. From the macroscopic theory point

of view, it represents the spatial distance over which the superconducting to normal transitions occurs. The coherence length is material dependent and a strong function of the lattice imperfections. Thus, the fundamental characteristic length, London penetration depth (λ_L), and Coherence length (ξ) were brought into light, which defines the behavior of a superconductor. Superconductors with $\xi > \lambda_L$ are called Type I, while Type II superconductors have $\xi < \lambda_L$ [14].

1.1.2 BCS theory

Even though GL theory was able to explain certain properties of superconductors by introducing the spacial dependent order parameter, the theory failed to address observations such as the appearance of a gap in the energy spectrum of superconductors, the exponential rise in heat capacity near T_c, and the isotope effect where $T_c \propto M^{-1/2}$, where M is the atomic mass of the isotope [15]. The existence of the energy gap hinted a phase transition in which there was a kind of condensation, like a Bose-Einstein condensation, while the evidence for electron-phonon interaction for forming the superconducting phase came from the isotope effect [10].

In 1957, a complete microscopic theory of conventional superconductivity was developed by Bardeen-Cooper-Schrieffer (BCS) based on the experimental observations mentioned above [16]. From a microscopic perspective, the electron's uncorrelated motion is responsible for conduction in normal state. However, in the superconducting state, all Cooper pairs condense in momentum space causes the loss of individual microscopic degree of freedom associated with each electron (fermion). A collective macroscopic coordinate such as the center of mass (CM) of the condensate governs the system's dynamics. The Cooper pairs' net momentum remains zero in the condensate as discussed in section 1.2. Furthermore, the zero resistance is possible due to the unique macroscopic collective quantum behavior of super electrons, described by a single coherent wavefunction that extends over the superconductor's volume.

The main idea behind the BCS theory is the concept of Cooper pairs. According to the BCS theory, the attractive interaction between electrons to form Cooper pairs (bosons) is phonon-mediated (lattice vibration). When an electron moves through a crystal lattice, due to Coulomb attraction, the lattice gets deformed, creating a region of higher positive charge density around the moving electron's vicinity. The magnitude of the lattice deformation depends on the isotopic mass of the positive ions, and the larger the ions mass lesser the development of the positive charge density. This electron-phonon interaction makes the second electron energetically favorable to move closer to a higher positive charge area, creating an effective, attractive interaction between the two electrons. This net interaction results from an interplay between the attractive phonon-mediated interaction and the repulsive screened Coulomb interaction. This correlated pair of electrons have opposite spin and momentum and is referred to as a Cooper pair and can move through the crystal lattice without resistance when all Cooper pairs form a condensate. The correlation appears to be of a long-range (at the scale of coherence length) of the order of several nm, and the energy of the pairing interaction is relatively weak, of the order of 10^{-3} eV depending on the material properties [10]. Thus, the Cooper pairs being bosons can condensate into the same zero momentum quantum ground state, which gives rise to the superconducting state which is protected by the superconducting energy gap (Δ). The superconducting state can cease when sufficient energy is supplied to break Cooper pairs. The thermal energy from the crystal lattice's vibrations (implies the existence of a critical temperature of T_c), magnetic energy from the magnetic field (suggests the presence of a critical magnetic field H_c) or large kinetic energy associated with high current density can break Cooper pairs and thus destroys superconductivity.

BCS theory uses mean-field theory to introduce the effective phonon mediated weak electron-electron (e-e) interaction of the form

$$V_{\text{eff}}(\omega) = |g_{\text{eff}}|^2 \frac{1}{\omega^2 - \omega_D^2}, \tag{1.5}$$

where, g_{eff} is an effective constant of electron-phonon interaction and ω_D is a cut-off frequency, above which the interaction becomes repulsive [10]. For $\omega < \omega_D$, phonon mediated interaction is constant and attractive, $V_{\text{eff}}(\omega) = -|g_{\text{eff}}|^2$, which produces Cooper pairing and causes the energy gap in the density of electron states at T and relates to T_c as

$$\Delta(0) \simeq 2\hbar\omega_D \exp\Big(-\frac{1}{N(\varepsilon_F)g_{\text{eff}}}\Big) \simeq 1.76 k_B T_c, \tag{1.6}$$

where $N(\varepsilon_F)$ refers to the electrons density of states at the Fermi surface. The BCS formula, Eq. (1.6) is valid only in the limit $N(\varepsilon_F)g_{\text{eff}} << 1$, in the so-called weak electron-phonon interaction regime and holds for most of the conventional superconductors. Physically, the energy gap is one-half of the minimum value of energy require to break a Cooper pair into two ordinary electrons. The natural explanation of the isotope effect comes from the relation $T_c \propto \omega_D \propto M^{-1/2}$, in agreement with the experimental observation. The most significant prediction of the BCS theory is that $\Delta(0)/k_B T_c \simeq 1.76$ takes the universal constant independent of material for all weak-coupling superconductors [10].

1.2 Josephson effect

The fundamental concept of quantum mechanics, the wave nature of particles, successfully explains the quantum tunneling phenomena observed in various fields of science. The detailed understanding of quantum tunneling has led to many applications such as electron tunneling in the field-effect transistor, the scanning tunneling microscope (STM), and the single-electron transistor (SETs) [17–19].

Tunneling of electrons and Cooper pairs can occur through different types of junction structures. Junctions can be formed by connecting two electrodes by a thin barrier layer. The electrodes can

be superconductors (S), normal metals (N), or the combination of a normal metal and a superconductor. The barrier layer can be a thin native oxide, an artificial oxide layer, a semiconductor, or a ferromagnetic material [20]. These structures have provided a platform to study the fundamental physics of the Josephson effect, Andreev reflection, Coulomb blockade, and even solid-state refrigeration and thermometry [21–25]. Our focus here is on the tunneling of electrons/Cooper pairs between the superconducting electrodes separated by a thin insulating layer (I). Thanks to Brian D. Josephson and Ivar Giaever for providing a clear theoretical understanding and experimental knowledge of physics behind the Josephson effect [26, 27].

Two superconductors connected by a thin insulating layer (S-I-S) are called a Josephson tunnel junction (JJ). According to BCS theory, at low temperature, a superconductor is a macroscopic quantum object described by a single quantum state occupied by all Cooper pairs. The macroscopic wavefunction representing the state of all Cooper pairs decays exponentially outside of the superconductor. When two superconductors are separated by a macroscopic distance (thick insulating layer), they behave as two independent quantum objects described by two individual superconducting order parameters. However, when the thickness of the insulating layer is gradually reduced coupling between the two superconductor electrodes can occur. The exponential tails of the order parameter of the superconducting electrodes overlap inside the thin insulating layer, enabling Cooper pair tunneling. Significant coupling can be created between the superconducting electrodes by fabricating junctions with a thin insulating layer ($\sim$ nm scale). This phenomenon is known as the Josephson effect [28].

Josephson theoretically predicted the "Josephson effect," which involves Cooper pair tunneling and manifests in two unique phenomena. First, the DC Josephson effect describes Cooper pairs' dissipationless tunneling, allowing one to observe a tunneling current at zero voltage. Second, the AC Josephson effect describes the transfer of Cooper pairs across the tunnel barrier, when there is a finite voltage (V) across the junction, via emitting a photon of energy $E = h\nu$ and therefore acts

as a perfect voltage to frequency (ν) converter $2eV = h\nu$, where e denotes the elementary charge and h is Planck's constant [29].

It is a good idea to recall a straightforward derivation of the Josephson relations done by Feynman,

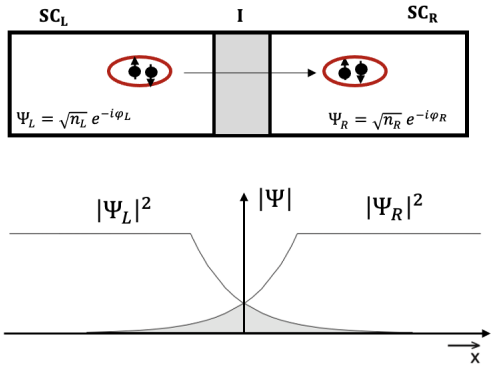

Figure 1.1. Schematic of a typical trilayer sandwich-type superconducting tunnel Josephson junction (S-I-S). Ψ_L and Ψ_R are the order parameters for the left (SC_L) and the right (SC_R) ground state of the superconductor electrodes respectively. The amplitude of the order parameter decays exponentially inside the insulator (I). The overlap of the order parameters inside the insulator provides a coupling between them and allows the Cooper pairs' tunneling. The supercurrent flow is along the x-axis.

which is based on a "two-level system" picture of a macroscopic quantum object [1, 30]. Without going into the full derivation, the Josephson relations can be obtained from the time evolution of the coupled "two-level system" described by the Hamiltonian, $H = H_L + H_R + H_I$. Here, H_L and H_R are the unperturbed Hamiltonian of the ground states of the respective superconductor, whereas H_I is the interaction Hamiltonian. The interaction Hamiltonian is written in terms of the coupling constant K as $H_I = K[\langle L|R\rangle + \langle R|L\rangle]$, where $|L\rangle$ and $|R\rangle$ are the condensate state vectors respectively. It measures the interaction between the two superconductors, which depends on the specific properties such as geometry, type of barrier, etc., of the junction. Assuming the two superconducting electrodes to be same, $|\Psi_L| = |\Psi_R| = \sqrt{n_s}$, and setting $\varphi = \varphi_L - \varphi_R$, we get the following

equations:

$$I = I_c \sin(\varphi) \tag{1.7a}$$

$$\frac{\partial \varphi}{\partial t} = \frac{2e}{\hbar} V = \frac{2\pi}{\Phi_0} V, \tag{1.7b}$$

where $\Phi_0 = h/2e$ is the flux quantum and $I_c = 2K/\hbar n_s$ is known as critical current, i.e., maximum supercurrent that can pass through the junction. As $I_c \propto K$, it reflects the coupling strength between the superconducting electrodes. The tunnel barrier thickness (d), typically on the order of a few nm (less than the superconducting coherence length), is required for the superconductor electrodes to remain phase coherent and to produce high J_c because of the exponential dependence of I_c on the tunnel barrier thickness (d). The Ambegaokar-Baratoff relation gives the magnitude of I_c in the case of an S-I-S junction

$$I_c(T) = \frac{\pi \Delta(T)}{2eR_N} \tanh\left[\frac{\Delta(T)}{2k_B T}\right], \tag{1.8}$$

where R_N is the normal state resistance of the junction [29]. Eq. (1.8) shows I_c depends on T and the superconducting energy gap Δ. The $I_c R_N$ product of a tunnel Josephson junction does not depend on the properties of a particular insulating barrier and at $T = 0$ is simply related to the superconducting gap as $V_c = I_c R_N = \pi\Delta(0)/2e$. Larger the gap, higher would be the characteristic voltage V_c. Thus, Eqs. (1.7a) and (1.8) describes the zero voltage DC properties of S-I-S Josephson junctions.

Eq. (1.7b) suggests that for $V \neq 0$ the phase varies in time as $\varphi = \varphi_0 + (2e/\hbar)Vt$ and therefore there exists an alternating supercurrent

$$I = I_c \sin\left(\varphi_0 + \frac{2e}{\hbar} Vt\right), \tag{1.9}$$

oscillating with a frequency $f = 2eV/h$. This is called the AC Josephson effect. The proportionality factor between voltage and frequency is referred to as the Josephson constant, $f/V = 2e/h =$

483.6 THz/V [31]. This forms the basis for the definition of the volt and the Josephson voltage standard. The inverse AC Josephson relation was confirmed experimentally by Shapiro. He observed the current steps (Shapiro steps) in the I-V curve by irradiating the junction with microwave of frequency ν. The current steps are observed at well-defined constant voltage values, $V_n = nh\nu$, known as Shapiro steps [32]. Further, Rowell studied the effect of magnetic field **B**, applied in the plane of S-I-S junctions. He observed the modulation of critical current I_c, analogous to the Fraunhofer pattern in a single slit optical diffraction experiment. This observation is a confirmation of the sinusoidal current phase relation and the uniformity of the junctions [28].

From an electrical circuit point of view, a Josephson junction is a dissipationless nonlinear inductor. This unique property makes tunnel junction a fundamental electronic component for the superconducting qubits (artificial atoms). The Josephson inductance $L(\varphi)$, instead of being a constant, can be modulated by the current passing through it. The dependence of $L(\varphi)$ on the bias current (I) can be obtained by differentiating Eq. (1.9)

$$L(\varphi) = V\left(\frac{dI}{dt}\right)^{-1} = \frac{\Phi_0}{2\pi I_c \cos\varphi} = \frac{\Phi_0}{2\pi I_c}\left[1 - \left(\frac{I}{I_c}\right)^2\right]^{-1/2} \tag{1.10}$$

Since it behaves as an inductor, an essential property of a Josephson junction is the capability to store energy from the tunneling of Cooper-pairs, known as Josephson energy E_J. The Josephson energy can be derived by taking the time integral of the power put into the junction, as follows:

$$W_J = \int IV\,dt = \int I_c \sin\varphi \frac{\hbar}{2e}\frac{d\varphi}{dt}dt = -E_J \cos\varphi, \tag{1.11}$$

where $E_J = I_c\Phi_0/2\pi$ is the maximum Josephson energy. It is clear that the energy stored in a JJ depends on φ. The non-linearity of Josephson energy is extremely important to superconducting circuits. Similarly, two conductors separated by a thin insulating layer act as a capacitor. The energy store by the capacitive channel is associated with the charging energy $E_C = e^2/2C$, where C is the junction's capacitance. Note that the ratio between E_J and E_c govern the Josephson junction's

behavior when designing different types of superconducting qubits.

1.3 RCSJ model

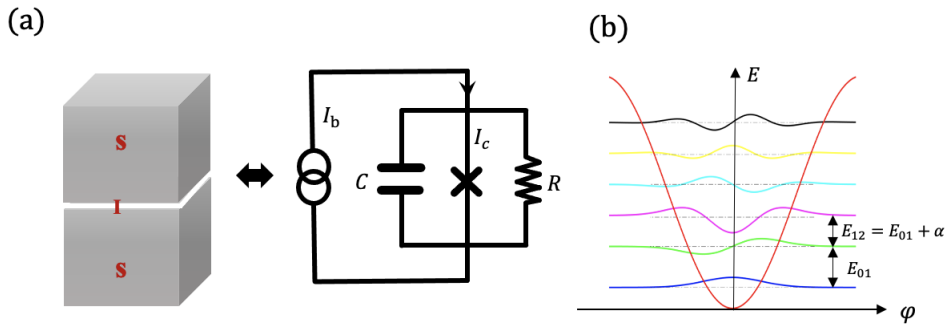

Figure 1.2. (a) A circuit diagram for resistively capacitively shunted Josephson junction model (RCSJ). The Josephson junction is modeled by an equivalent electronic circuit consisting of a Josephson inductor in parallel with an ohmic resistor R and a capacitor C. (b) The Josephson junction has the cosine potential energy, which gives rise to the unevenly spaced energy levels.

The resistively and capacitively shunted junction model (RCSJ model) introduced by Stewart and McCumber in 1968 [33, 34] is successful in explaining the phase dynamics of Josephson junction. The junction is modeled by an equivalent electronic circuit consisting of a Josephson inductor in parallel with an ohmic resistor R, which represents its effective shunt resistance accounting for the dissipation due to the presence of quasiparticles in the finite voltage state, and capacitor C accounting for the intrinsic capacitance (geometry dependent) arising from junction's superconducting electrodes as shown in FIG. 1.2(b). The dissipation here is modeled as a frequency-independent resistance, which accounts for other normal conduction channels parallel with the junction. The current across the junction can be written as the sum of the currents through the three components

as

$$I = I_c \sin\varphi + \frac{V}{R} + C\frac{dV}{dt}. \tag{1.12}$$

We can express the equation in terms of phase by using Josephson relations, Eq. (1.7b).

$$I = I_c \sin\varphi + \frac{\hbar}{2eR}\frac{d\varphi}{dt} + \frac{\hbar C}{2e}\frac{d^2\varphi}{dt^2} \tag{1.13}$$

The dimensionless form of the equation, which has the advantage of reducing the number of system parameters, is

$$i = \sin\varphi + \frac{d\varphi}{d\tau} + \beta_C \frac{d^2\varphi}{d\tau^2}, \tag{1.14}$$

where $i \equiv I/I_c$ is the normalized bias current, $\tau = 2eI_cRt/\hbar$, and $\beta_C = 2eI_cR^2C/\hbar$ is called Stewart-Macumber parameter, which determines the type of I-V characteristic of the junction.

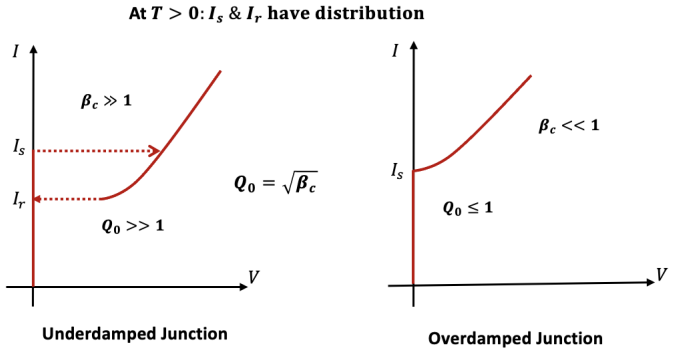

Figure 1.3. The schematic I-V characteristics showing the typical hysteretic ($\beta_C >> 1$) and non-hysteretic ($\beta_C << 1$) behavior of a Josephson junction. I_s and I_r are the switching and re-trapping current respectively. The Stewart-Macumber parameter, β_C is related to the quality factor as $\beta_C = Q_0^2$.

When the junction is underdamped, $\beta_C >> 1$, the I-V curve is hysteretic. The tunnel-junction-like hysteresis has the presence of abrupt switching from the zero to the finite voltage state hence is convenient for measuring switching current distribution (SCD). In contrast, for overdamped junctions $\beta_C << 1$ the I-V characteristics are nonhysteretic. In this case, switching from the superconduct-

ing state (zero voltage state) to the normal state (finite voltage state) is continuous hence it is much harder to determine switching current accurately.

Based on the RCSJ model, the dynamics of a current biased Josephson junction is analog to a fictitious phase particle of mass C moving in a washboard potential

$$U(\varphi) = \frac{I_c \Phi_0}{2\pi}\left(-\frac{I}{I_c}\varphi - \cos\varphi\right) = -E_J(i\varphi + \cos\varphi), \tag{1.15}$$

where C is the junction's shunt capacitance, and φ is the gauge-invariant phase difference across the junction representing position of the phase particle. The potential has the form of a tilted cosine, for which the tilt is proportional to the normalized bias current i and is therefore called a washboard potential. FIG. 1.4 shows a plot of $U(\varphi)$ at several values of the normalized bias current i. Between $\varphi = 0$ and 2π, the washboard potential has a local minima located at $\varphi_{\min} = \sin^{-1} i$

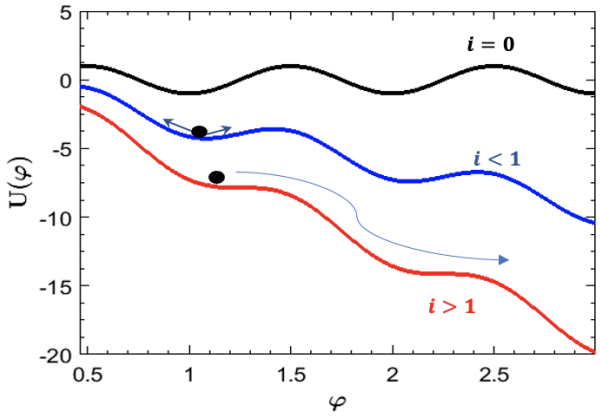

Figure 1.4. The washboard potential of a Josephson junction plotted for three different tilt controlled by the ratio I/I_c. A solid black sphere shows the fictitious phase particle at one of the potential minima, which oscillates with the small oscillation frequency ω_p at the bottom of the well.

and a maxima at $\varphi_{\max} = \pi - \sin^{-1} i$. The barrier height of the metastable potential well for $i < 1$ is given by [35]

$$\Delta U = U(\varphi_{\max}) - U(\varphi_{\min}) = 2E_J\left(\sqrt{1-i^2} - i\cos^{-1} i\right). \tag{1.16}$$

When $i = 0$, the barrier height becomes maximum $\Delta U \equiv 2E_J$ which shows Josephson energy E_J as the characteristic energy scale involved in the phase dynamics. The barrier height, ΔU can be fine-tuned by varying i and for $i \to 1$ is given by

$$\Delta U \cong E_J \frac{4\sqrt{2}}{3}(1-i)^{3/2}. \tag{1.17}$$

In the experiment, the bias current I is close to I_c; under this approximation, the shape of the potential is cubic. The anharmonicity, which leads to a decrease in the spacing of the energy levels in the well with increasing energy, is crucial to observe ELQ. When the phase particle is trapped in one of the potential wells, it undergoes a small oscillation at the bottom of the potential well. The angular frequency of the oscillation can be obtained by knowing the potential's curvature.

$$\omega_p = \sqrt{\frac{U''(\varphi)}{m}} = \omega_{p0}(1-i^2)^{1/4} \equiv \sqrt{\frac{2\pi I_c}{C\Phi_0}}(1-i^2)^{1/4}, \tag{1.18}$$

where $\omega_{p0} = \sqrt{2\pi I_c/\Phi_0 C}$ is the plasma frequency at zero bias current. For a typical tunnel junction, the plasma frequency is in the microwave range, with several tens of GHz.

The quality factor (Q_0) is the ratio of energy stored to the energy dissipated per cycle. The value of Q_0 approximates the number of periods it takes to dissipate the energy stored in an oscillator. For Josephson junctions, Q_0 is the figure of merit that measures the damping of the system by the shunt resistance R and is defined as $Q_0 = \omega_{p0}RC$. Josephson junctions fall into three different damping regimes: under-damped ($Q_0 >> 1$), moderately damped ($1 < Q_0 \lesssim 5$), and over-damped ($Q_0 \leq 1$). Although the RCSJ model predicts many properties of the Josephson junction correctly and straightforward, one should be aware of the fact that the model is simplified by assuming a frequency-independent shunt resistance, which neglects any contributions to the junction impedance at high frequencies arising from the bias circuitry [36–38].

1.4 Escape from a metastable potential well

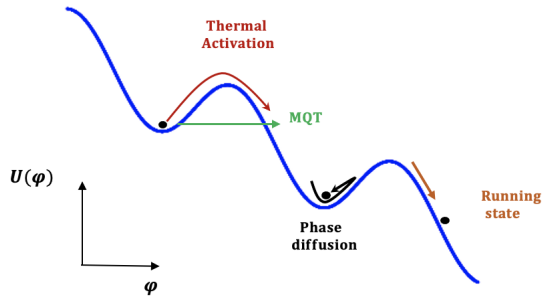

Figure 1.5. Washboard potential showing different escape mechanisms. There are three states a phase particle can be in the washboard potential. Trapped ($V = 0$), intermediate PD (tiny V), and the running state (finite V). The phase particle escapes from the initial potential well (trapped state) by thermal activation (TA) or macroscopic quantum tunneling (MQT), depending on the temperature. There are two subsequent motions of the phase particle in the washboard potential after the initial escape: (1) direct to the running state; (2) via PD to the running state. In the later subsequent motion, phase particle suffers multiple escapes and retraps in the subsequent potential wells before transiting to the full running state. This multiple escapes and retraps of the phase particle give rise to a diffusive motion called phase diffusion (PD).

The I-V curve of the Josephson junction shows that there are two states: (1) the superconducting state (zero voltage state) and (2) the normal state (finite voltage state). In terms of washboard potential, they correspond to the fictitious phase particle being in a trapped state ($V = 0$) and running state (finite V), respectively. A phase particle is in a trapped state if it always remains in the initial metastable potential well. On the other hand, in the running state, i.e., after an initial escape, the phase particle steadily runs down the washboard potential without hindrance. Besides that, there is an intermediate PD state (tiny V): after escaping from the initial potential well, the phase particle suffers from repeated retrapping and escape in the subsequent potential wells before going to the full running state as i (thus the tilt) is increased. Thus, there are two distinctive transiting sequences from the trapped state to the running state: (1) Direct; (2) via PD.

To understand escape mechanism's from the initial potential well, let us zoom to a particular metastable well as shown in FIG. 1.5. At $T = 0$ and $i < 1$ (maximum ΔU), the phase particle has an infinite lifetime ($\tau = 1/\Gamma$, where Γ is the escape rate) in the zero-voltage state (trapped state). However, in reality, the presence of quantum and thermal fluctuations ($\propto T$) allow the phase particle to oscillate at the bottom of the well with plasma frequency ω_p and the probability of escaping from the well is possible. Thus, there are two mechanisms of escape: thermal activation (TA) and macroscopic quantum tunneling (MQT) through which the phase particle can escape from a metastable potential well [39, 40].

1.4.1 Thermal activation (TA)

In the classical regime, the system's dynamics is described by the classical equation of motion Eq. (1.13), in which phase difference φ is a classical dynamical variable representing the position of the fictitious phase particle. In this regime, where $k_B T >> \hbar\omega_p$, a well-known theory for the escape rate was developed by Kramers [41]. Furthermore, it was applied to the case of washboard potential of current-biased Josephson junctions by Buttiker, Harris, and Landauer [42]. Due to thermal fluctuations, the phase particle could gain sufficient energy to escape from the potential well by climbing over the top of the potential barrier. The temperature-dependent thermal activation rate has the form of the Arrhenius equation:

$$\Gamma_{\mathrm{TA}} = a_t \frac{\omega_p}{2\pi} \exp\left(-\frac{\Delta U}{k_B T} \right), \tag{1.19}$$

where $a_t = (1+\alpha^2)^{1/2} - \alpha \in (0,1)$ is dimensionless damping dependent factor with $\alpha \equiv 1/2Q_0$. The importance of thermal activation theory lies in the fact that the escape rate decreases exponentially with the barrier height over temperature.

1.4.2 Macroscopic quantum tunneling (MQT)

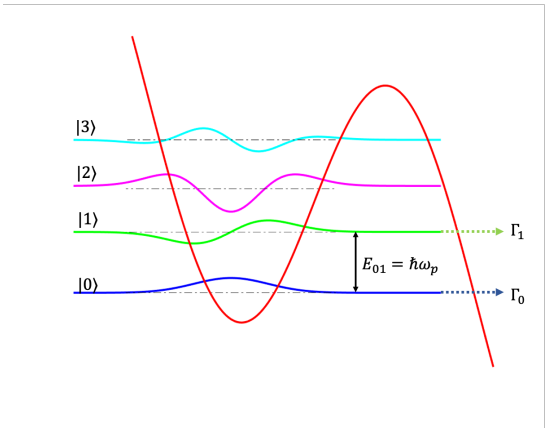

Figure 1.6. In the quantum picture, the phase particle dynamics are described by a wave function $\Psi(\varphi)$, and the energy of the particle takes discrete values indicated as grey horizontal lines. Each state is shown with the corresponding squared wavefunctions $|\Psi|^2$. The phase particle in the excited state $|1\rangle$ sees the barrier height reduced by the energy difference E_{01}. Hence the tunneling from the excited state occurs at a rate Γ_1 which is exponentially larger than the tunneling rate from the ground state Γ_0.

In the quantum regime, $\hbar\omega_p >> k_B T$, the dynamics of the phase particle is described by quantum mechanics. The phase difference φ is a quantum mechanical operator rather than a classical variable. The phase particle behaves as a quantum mechanical object with its state described by a wave function, $\Psi(\varphi)$, and the phase particle's energy takes discrete values as shown in FIG. 1.6. Hence, quantum mechanics allows the wave to leak out of the potential barrier. This leakage of $\Psi(\varphi)$ enables the phase particle to escape from the potential well by macroscopic quantum tunneling (MQT) through the barrier [36, 43]. In the limit of weak and moderate damping and $T = 0$ the MQT rate is given by

$$\Gamma_q = a_q \frac{\omega_p}{2\pi} \exp\left(-7.2 b_q \frac{\Delta U}{\hbar\omega_p} \right), \tag{1.20}$$

where $a_q \approx [120\pi(7.2\Delta U/\hbar\omega_p)]^{1/2}$ and $b_q \approx \left[1 + 0.87/Q_0 + O(Q_0^{-2})\right]$ [43, 44]. It is evident from Eq. (1.20) that the tunneling rate is independent of temperature ($\hbar\omega_p >> k_B T$). Furthermore, quantum mechanics predicts the presence of quantized energy levels in the potential well. The phase particle in the first excited state sees the barrier height reduced by $\hbar\omega_p$. Hence, the tunneling

rate Γ_1 is exponentially higher than the ground state rate Γ_0. In the experiment, difference between Γ_0 and Γ_1 enables one to observe energy level quantization (ELQ). The transition from classical thermal activation (TA) to quantum tunneling (MQT) occurs at a particular temperature called crossover temperature,

$$T_{\rm cr} = \frac{\hbar\,\omega_p}{2\pi k_B}. \tag{1.21}$$

The level of damping and the plasma frequency determine the temperature at which quantum effects take over [45, 46].

1.4.3 Phase diffusion (PD)

We understand that the phase particle can escape from the initial metastable potential well (trapped state) via TA or MQT. The relative weight of these two escape processes depends on the temperature of the system. After the initial escape the phase particle can enter two different states: (1) the running state; (2) the state of phase diffusion (PD), from which it can finally reach the running state as the potential is tilted further. In the latter case, the phase particle undergoes multiple retraps and escapes in the subsequent potential wells before transitioning to the running state. The multiple retraps and escapes of the phase particle give rise to a diffusive motion called phase diffusion. There is no well established analytical rate equation to describe PD but it can be observed in experiment. Unlike escape mechanisms, PD and its transition to the running state has not been very well understood [47].

It has been recognized that junction parameters E_J/E_C and E_J/T, strength of damping, and thermal (quantum) fluctuations are the factors behind the phase particle's dynamics in the washboard potential [48–50]. However, role of bias current has not been appreciated previously. At higher temperature the phase particle would escape via TA, at lower bias currents which increase the

probability of retrapping in the subsequent wells. Thus, it is necessary to provide a larger tilt to the potential to allow the junction to switch from PD to the running state.

1.4.4 Switching current distributions (SCDs)

The rate of escape via TA and MQT are given by Eqs. (1.19) and (1.20). Switching current distributions can be obtained from the escape rate, if the current ramp rate, dI/dt, is known.

$$P(I) = \frac{\Gamma(I)}{dI/dt} \exp\left[-\frac{1}{(dI/dt)} \int_0^I \Gamma(I')dI' \right] \tag{1.22}$$

The mean and the variance of the distribution are

$$\langle I \rangle = \int IP(I)dI \tag{1.23a}$$

$$\sigma^2 = \int (I - \langle I \rangle)^2 P(I)dI. \tag{1.23b}$$

We studied the escape dynamics of Y-Ba-Cu-O planar Josephson junctions by the time-of-flight

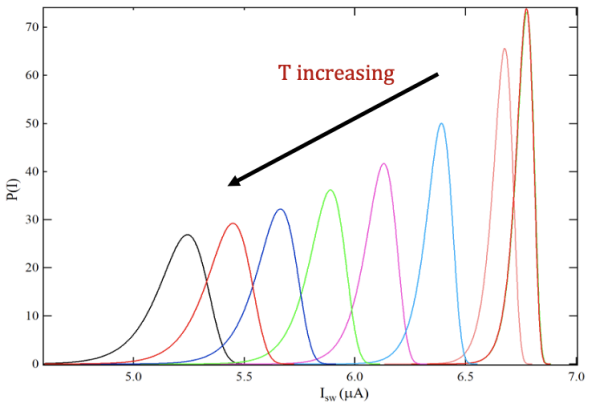

Figure 1.7. SCDs, $P(I)$, obtained from TA and MQT rate using Eq. (1.22). The SCDs overlap in MQT regime irrespective of the change in temperature.

technique [51, 52]. The bias current I is increased linearly in time from zero until the junction switches to the finite voltage state corresponding to the phase particle running down the tilted washboard potential landscape. The time, and thus the bias current, at which the junction switches to the running state is recorded. After each switching, $I(t)$ is returned rapidly to zero. This process is repeated for a large number (e.g., 10^4) of times to have good statistics.

The SCDs overlap in the MQT regime irrespective of the temperature change which can be seen as a saturation in mean $\langle I_s \rangle$ and width σ, i.e., $d\langle I_s \rangle / dT$ and $d\sigma/dT = 0$. At $T < T_{cr}$ the mean and width become nearly T-independent and their values are determined uniquely by the junction's parameters (I_C, C, R) and to a much lesser extend by the rate of bias current sweep. Notice that experimental artifacts, such as extrinsic current noise and joule heating, could also cause the mean and width to saturate at low temperatures. Therefore, caution must be taken to eliminate these artifacts.

In TA regime, the width of the SCDs has several distinctive characteristics: $\sigma \propto T^{2/3}$, $d\sigma/dT > 0$, and highly asymmetric $P(I)$. While in PD regime $d\sigma/dT < 0$ and the SCDs become symmetric. Furthermore, as T increases, the skewness, $\gamma_3 = \mu_3/\sigma^3$, where μ_3 is the third moment of the distribution becomes less negative and ultimately goes to zero when PD is prevalent [38, 52, 53].

1.5 SQUID as flux logic device

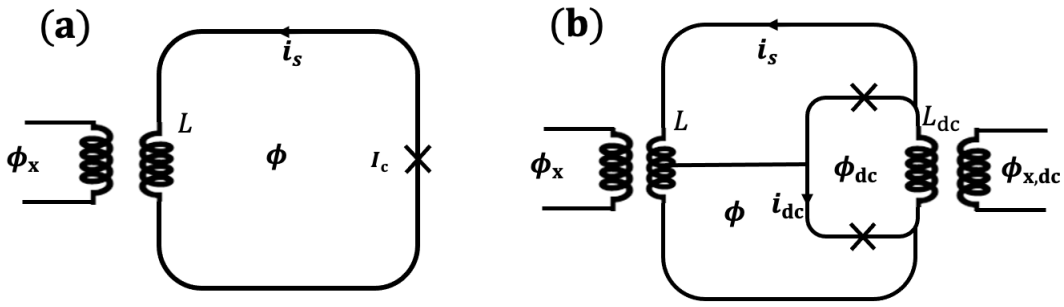

Figure 1.8. (a) Schematic circuit diagram of rf-SQUID with a dynamical variable as the total magnetic flux Φ and external flux Φ_x which modulates the potential. L is the superconducting loop's inductance, while I_c is the junction's critical current. (b) The modification introduced to tune the critical current *in situ* by replacing a single junction with two junctions in a small loop, a dc-SQUID, with inductance L_{dc}.

An rf-SQUID is a superconducting ring interrupted by a Josephson junction, as shown schematically in FIG. 1.8(a). The junction is characterized by its critical current I_c, shunt capacitance C, and shunt resistance R according to the RCSJ model. When an external flux Φ_x is applied to the superconducting loop, it induces a persistent current $i_s = -I_c \sin(2\pi\Phi/\Phi_0)$. The total flux in the loop must satisfy $\Phi = \Phi_x + Li_s$ where L is the geometrical inductance of the loop. The dynamics of this device is analog to a fictitious flux particle of mass 'C' with kinetic energy $C\dot{\Phi}^2/2$ moving in a potential given by the sum of the magnetic energy and the Josephson energy [54, 55]. In term of normalized flux $\phi = \Phi/\Phi_0$ the potential is given by

$$U(\phi) = U_L \left[\frac{(\phi - \phi_x)^2}{2} - \frac{\beta_L}{4\pi^2} \cos(2\pi\phi) \right], \tag{1.24}$$

where, $U_L = \Phi_0^2/L$ sets the overall energy scale of the potential while $\beta_L \equiv 2\pi LI_c/\Phi_0$ and $\phi_x \equiv \Phi_x/\Phi_0$ determine the shape of the potential. When $\phi_x = 1/2$ and $1 < \beta_L \lesssim 4.6$ the potential is symmetric about $\phi = 1/2$ with two wells separated by a potential barrier. The two potential wells

correspond to two fluxoid states of the rf-SQUID, with currents circulating in opposite directions around the loop. Changing ϕ_x slightly away from $1/2$ tilts the potential, which results in an energy bias $\varepsilon \propto \phi_x$ between the two fluxiod states.

The problem with this design is that the circuit parameters such as the height of the symmetric double-well potential ΔU_0 and the tunnel splitting Δ, which are important to observe macroscopic quantum phenomena, cannot be tuned *in situ* [56]. To solve this problem, the single junction is replaced by two junctions in a small loop, a dc-SQUID, with inductance L_{dc} such that $L >> L_{dc}$ as shown in FIG. 1.8(b). If $\Phi_{x,dc}$ is the flux applied to the dc-SQUID loop then $\Phi_{dc} = \Phi_{x,dc} + L_{dc} i_{\rm dc}$ where $i_{\rm dc}$ is the current circulating the dc-SQUID loop. This system's macroscopic dynamical variables are the magnetic fluxes Φ through the qubit loop and Φ_{dc} through the dc-SQUID loop [57]. Thus the tilt and the barrier height of the two-dimensional potential energy landscape can be controlled independently. In the limit of $L/L_{dc} >> 1$, the modified circuit can be approximated by Eq. (1.24) with the parameter β_L replaced by

$$\beta_L(\phi_{x,dc}) = \beta_{L0} \cos(\pi \phi_{x,dc}), \tag{1.25}$$

where $\beta_{L0} \equiv 2\pi L I_c/\Phi_0$. The system is analog to a fictitious flux particle moving in a 1D double-well potential. A SQUID can be thus used as a one-bit logic device having two discrete states, "-1" and "1" corresponding to the flux particle in the left and right well, respectively. Note that the flux logic device has a high characteristic frequency, $\omega_{\rm p}/2\pi \sim 10^{10}$ Hz, which makes it an excellent candidate for realizing a high-efficiency Szilard engine with unprecedented performance [58].

1.6 Organization of the dissertation

This dissertation's structure is as follows: Chapter 2 begins with a brief discussion of macroscopic quantum tunneling (MQT) and its importance. Then, the motivation to use high-T_c Y-Ba-Cu-O nano-JJs. Next, the experimental techniques and the measurement setups employed to investigate the quantum behavior of such junctions is discussed. Finally, the chapter is concluded with the result of T dependence of the switching current distribution (SCD) measurement of these junctions in the Oxford dilution refrigerator.

In Chapter 3, PD in nano Y-Ba-Cu-O Josephson junction is discussed. We present our finding that retrapping is prevalent at small bias currents, which leads to PD at small current biases. The chapter is concluded by demonstrating the importance of potential tilt through the phase diagram.

In Chapter 4, SQUID-based flux logic device as a Szilard engine is investigated. The performance of the Szilard engine is optimized in terms of speed and power, via numerical simulation. The results demonstrate that Szilard engine's performance can exceed that of other nano-device implementations by orders of magnitude.

Finally, in Chapter 5, the dissertation concludes with a summary of the main results, outlooks and direction for future works.

Chapter 2

Escape from metastable potential

In this chapter we report unambiguous experimental evidence of MQT in Y-Ba-Cu-O planar Josephson junctions fabricated by the focused helium ion beam method [59–65].

2.1 Macroscopic quantum tunneling (MQT) in Josephson junctions

In 1980, Anthony Leggett emphasized that the macroscopic variable such as the flux (Φ) of an LC oscillator should obey quantum mechanics [66]. He pointed out two crucial requirements the system must satisfy in order to exhibit quantum behavior. First, the system must be sufficiently cold such that $\hbar\omega_p >> k_B T$, which ensures that quantum fluctuation is dominant. Second, the quantum state's lifetime must be long enough to be measured ($Q_0 >> 1$) [67]. However, even if an LC oscillator satisfies the requirements mentioned earlier, its energy levels are equally spaced due to quadratic potential, causing no difference between classical and quantum responses to an external sinusoidal perturbation. Later, it was demonstrated that by replacing the LC resonator's linear inductor with the non-linear Josephson inductor, the system becomes anharmonic oscillator with the phase (φ) across the Josephson junction as the macroscopic quantum variable [68]. Quantum mechanics allows the wave function to extend through the barrier allowing phase particle to escape from the potential well by macroscopic quantum tunneling. Thus, the theoretical work done by

Anthony Leggett showed the possibility of observing macroscopic quantum tunneling (MQT) of the phase particle and energy level quantization (ELQ) in an electronic circuit [44].

In 1981, Voss and Webb [69] measured the temperature dependence of probability distributions for switching out of the superconducting state of 1-μm Nb Josephson junctions for the first time and presented compelling evidence for quantum tunneling of a macroscopic variable. They found that the experimental results agree well with the theory derived by Caldeira and Leggett [43, 66]. Later experiments have addressed the effect of environment (damping) and finite temperature on macroscopic quantum tunneling [70–72].

Furthermore, Devoret, Martinis, and Clarke thoroughly investigated quantum behavior of current bias Josephson tunnel junctions [67]. Their result demonstrated MQT and provided evidence of energy level quantization (ELQ) in Josephson junctions. These experiments, along with a few significant others [40, 44, 68, 70], had become the manifestations of the quantumness of macroscopic variables. Thus, observation of MQT and ELQ in superconducting Josephson junctions have paved a way to test macroscopic quantum effects such as macroscopic resonant tunneling (MRT), photon assisted tunneling, macroscopic quantum coherence (MQC), etc., and has led to architect a variety of artificial atoms i.e., qubits [56, 73, 74].

Since a part of the dissertation focuses on studying MQT in high T_c Josephson junctions, I would like to recall some of the field's crucial achievements. Studies of cuprate superconductors show that they have anisotropic superconducting properties and are built on complex material structures. Due to the presence of nodes in the d-wave order parameter of the cuprates, there are always low energy quasiparticles responsible for enhancing dissipation which suppresses MQT in HTS devices [75–77]. Aside from these complications, evidence of MQT in HTS JJs has been reported by many groups [78–80]. Bauch *et al.* and L. Longobardi *et al.* reported for the first time the observation of MQT in Y-Ba-Cu-O grain boundary biepitaxial JJs [77, 79]. MQT has also been observed in

c-axis oriented intrinsic junctions made from single-crystal Bi-2212 [52, 81–84].

Superconducting quantum circuit has attracted extensive attention because of its importance to the investigation of basic concepts in quantum mechanics [43, 68, 69] and its prominent role in quantum information processing [85–87]. Although significant progress in coherence time and numbers of entangled qubits have been made in the past two decades, seeking new materials that could improve the coherence time of superconducting quantum circuits and scalable nanofabrication processes are actively pursued [88–90]. Recently, cuprate superconductor planar Josephson junctions fabricated by FHIB direct-writing exhibits promising properties, and reproducibility [61, 91, 92]. In this method, a crystalline nano-scale barrier is created in a single layer superconducting thin film to form a Josephson junction by irradiation of a 0.5-nm FHIB, which is one of the most straightforward and scalable ways to make circuits containing a moderately large number of Josephson junctions [93]. To demonstrate quantum nature of this new type of Josephson junctions for quantum circuit applications, macroscopic quantum tunneling (MQT) is the essential first step [37, 38, 79].

2.2 HTS Josephson junction

The search for high-T_c superconductors (HTS) are motivated to find new materials which can possibly superconduct at room temperature and have high critical field and critical current density that would lead to significant changes in the technological applications. $YBa_2Cu_3O_{7-\delta}$ (Y-Ba-Cu-O) was the first ceramic material discovered to superconduct at a temperature above the boiling point of liquid nitrogen (77 K). The advantage comes in lowering the cost of large-scale applications because compared with liquid helium nitrogen is much more abundant much cheaper, and readily available [94].

The major advantage of HTS is that they have large superconducting energy gap corresponding

to several THz. HTS JJs mostly have non-hysteretic *I-V* characteristics, and high characteristic frequency $f_c = I_c R_N/\Phi_0$ which are required for high-speed digital circuits (RSFQ) and microwave circuits. Also, HTS have the ability to sustain the superconducting state and to carry higher J_c in large magnetic fields. This property makes them suitable for high field applications [95].

Material	T_c (K)	Δ (meV)	λ (nm)	ξ (nm)	H_c (T)
Al	1.2	0.2	16.0	1600	0.01
Nb	9.3	1.5	44.0	40	H_{c1} ~0.2; H_{c2} ~0.3
Y-Ba-Cu-O	93	20-25	λ_L^{ab}=150-300; λ_L^{c}=1000	ξ^{ab}=1-4; ξ^{c} ~0.7	H_{c2}^{ab}=250; H_{c2}^{c} ~120

Table 2.1. Main superconducting parameters for Type-I (Al) and Type-II (Nb and optimally doped Y-Ba-Cu-O) materials [14, 95]. T_c is the critical temperature and Δ is the superconducting energy gap. λ_L and ξ are the London penetration depth and the coherence length, respectively, while H_{c2} represents the upper critical field. The HTS has anisotropic properties along *ab* plane and *c* axis distinguish as superscript in λ_L, ξ and H_{c2}.

The major obstacles to the application of cuprate high-T_c superconductors are: they have complex crystallographic structures and usually possess a layered structure, and they have anisotropic superconducting properties. The superconducting properties are notably different along the *c*-axis compared to in the *ab*-plane as listed in Table (2.1) [96, 97]. The essential material constraints to fabricate high-quality JJs are represented by the small and anisotropic coherence length, ceramic nature (brittle material) and the easy surface and interface degradation of HTS films [98, 99]. Apart from difficulties, different techniques are implemented to fabricate Y-Ba-Cu-O Josephson junctions suitable for superconducting electronics. The well known techniques used to fabricate HTS JJs include bicrystal, ramp-edge, and bi-epitaxial. A detailed study about their fabrication methods and characterization can be found in [100–104]. These methods lack the required stability, uniformity, and desirable reproducibility to make high-quality HTS junctions and SQUIDs [105]. Thus, researchers are in search of an advanced method to fabricate junctions and SQUIDs that can provide atomically precise material manipulation to the requirements demanded by various applications. Another major problem about HTS JJs is that the value of $I_c R_N$ has been consistently lower

than the energy gap (Δ) [61, 103]. So far, there is no well-established theory for the mechanism of superconductivity in these strongly correlated electron systems [75, 106]. The understanding of the microscopic mechanism of the cuprates superconductors is still an outstanding problem.

2.3 Experiment method

2.3.1 Cooling down to millikelvin (mK) temperature

In 1908, Kammerlingh Onnes, for the first time, succeeded to liquefy helium (He), which was later used to discover the superconductivity in mercury (Hg). Low-temperature physicists investigate exotic phenomena like Bose-Einstein condensates, superfluids, fractional quantum Hall effect, and superconductivity, whose energy scale is much smaller than the thermal energy at room temperature, $k_B T \approx 26\,\mathrm{meV}$. They require the use of liquid helium, which boils at $T = 4.2\,\mathrm{K}$, which corresponds to $\approx 0.1\,\mathrm{meV}$ of thermal energy. There are different cooling techniques to decrease temperature to below $4.2\,\mathrm{K}$. For example, by reducing the liquid helium's vapor pressure, one can reach $\sim 1.2\,\mathrm{K}$. One of the refrigerators that I have used is the physical properties measurement system (PPMS), which utilizes the evaporative cooling power of liquid helium, whose base temperature is $\approx 1.2\,\mathrm{K}$. Here, the cooling is achieved due to the latent heat of the evaporated liquid helium.

The quantum phenomena that we are interested in at least require a base temperature of $50\,\mathrm{mK}$ to observe. In addition, the quantum electronic circuits' operation requires temperatures on the order of 10 mK to initialize the systems in their ground state and avoid errors due to thermal excitation. Therefore, different refrigeration equipments have to be employed, such as the dilution refrigerators, which are multi-stage coolers based on circulating $\mathrm{He}^3 - \mathrm{He}^4$ [107].

The working mechanism of dilution refrigerator (DR) will be briefly described in the following. A more comprehensive explanation can be found in literature [108, 109]. Nature is kind enough to us

by providing the two isotopes of helium (He^3 and He^4) [110]. When a mixture of He^3 and He^4 is cooled to below 0.87 K (Tri-critical temperature), the mixture separates into two different phases, with one floating on the top of the other. He^3 being lighter creates a concentrated upper phase, whereas the more massive diluted phase at the bottom mainly contains He^4 plus a fraction (6 .4%) of He^3 [107]. The finite solubility of He^3 in He^4 is the key to dilution refrigeration. He^3 from the diluted phase can be removed due to its low vapor pressure, and this removal forces the He^3 from the concentrated phase to occupy the created vacant place in the diluted phase. The transfer of atoms from the pure phase to the diluted phase increases the system's entropy, which requires energy. Thus, heat is absorbed from the environment (sample) in the form of thermal energy during the process, which cools the sample in the long run. In a closed-loop operation, circulation pumps are used to continuously pump He^3 and return it into the concentrated He^3 phase. In this way, it is possible to generate sufficient cooling power for continuous refrigeration down to temperatures below 10 mK [111].

Even though Y-Ba-Cu-O Josephson junction becomes superconductor at $T_c = 93$ K MQT and ELQ usually would not be observed above a few kelvins because TA is the prevailing escape mechanism ($\hbar\omega_p >> k_B T$).

2.3.2 The measurement circuit

The current and voltage leads from room temperature to low temperature, which are used for current bias and the measurement of voltage across the junction, are composed of flexible coaxial cables, electromagnetic interference (EMI) filters, low pass RC filters, and LC-copper powder filters (LC-CPF) down to the sample platform. Measuring switching current can be performed by ramping up the bias current to slightly above I_c causing the junction to switch to the running state ($V \neq 0$), then reducing the bias current to zero to prepare for next measurement cycle. This is accomplished using an arbitrary waveform generator, AWG 33120A, which is programmed to

generate a triangular current bias waveform. The signal from the AWG goes through an isolation amplifier to the biasing (R_{bias}) and sensing (R_{sense}) resistors to the Josephson junction. To limit the current (order of 10 μA) to the range just necessary to causing the junction to switch, R_{bias} is set to 100 kΩ.

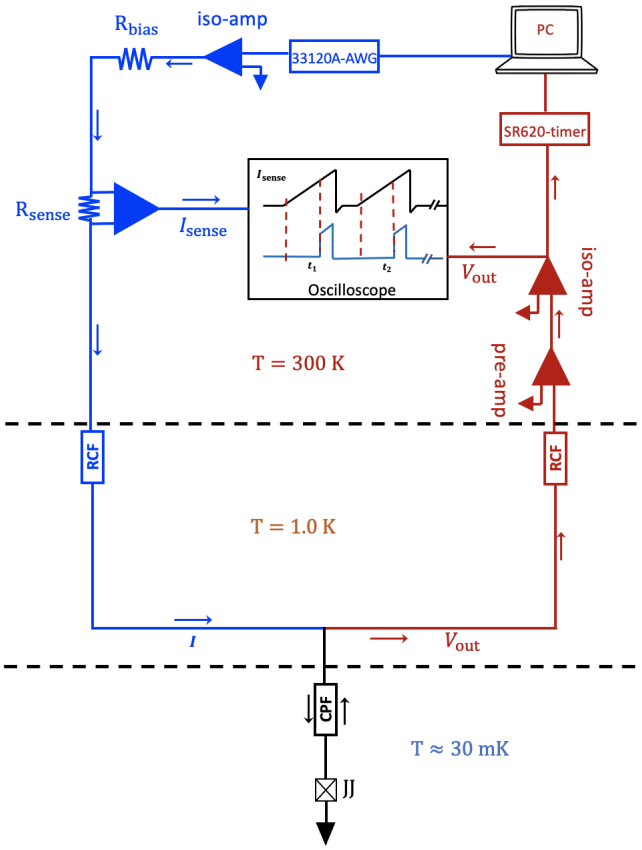

Figure 2.1. Schematic circuit diagram of the electronic measurement system for switching current distribution (SCD). The AWG-33120A is programmed to feed the bias current to the junction. The current passes through the low pass RC (RCF) and LC–copper powder (CPF) filters installed at different cryogenics plates to mitigate the noise. The voltage dropped across the junction is amplified and sent to the timer, SR620.

The value of R_{sense} is adjusted to give the maximum current sensitivity while keeping the voltage below the maximum input of the current sensing amplifiers. All amplifiers are kept inside an rf-shielded room to mitigate EM interference. The bias current is passed to the fridge through

flexible coaxial lines. The low-pass RC filters have cutoff frequency $\approx 100\,\mathrm{kHz}$, and are thermally anchored to the 1 K plate of the fridge. Finally, the bias current is applied to junctions through the LC-CPF maintained at the mixing chamber temperature. The homemade LC-CPF is designed to have a cut off frequency of about 80 MHz and provides more than 90 dB attenuation at frequency greater than 80 MHz. The junctions are protected from the stray magnetic field from the environment by the use of a Mu-metal magnetic shield at room T and a Cryoperm shield at 4.2 K reducing the residual magnetic field to the order of 50 nT [112].

The time-of-flight method is used to measure the SCDs [113]. When the finite voltage appears across the junction, the signal is passed to the room temperature amplifier and then fed to the timer SR620. The timer record the time interval between the beginning of the bias current waveform to the point when the junction suddenly switches to the $V \neq 0$ state. The information is recorded on the computer through a GPIB connection. All instruments used in the experimental setup should have a single ground to avoid the ground loops. To avoid heating, the ramp has been set to reduce the time the junction spends in the resistive state and a dwell time for $I = 0$ has been programmed to increase the time the junction spends in the superconducting state.

2.4 Results and discussion

The nano Josephson junction is characterized in an Oxford dilution refrigerator. A typical current-voltage (I-V) characteristics of the junction at 50 mK is shown in FIG. 2.2. The normal resistance $R_{\mathrm{N}} = 104\ \Omega$ is obtained from the linear part of the I-V curve at $|V| > 1$ mV. The quality factor of the junction Q_0 can be estimated from the degree of hysteresis of IVC and is calculated to be 1.4.

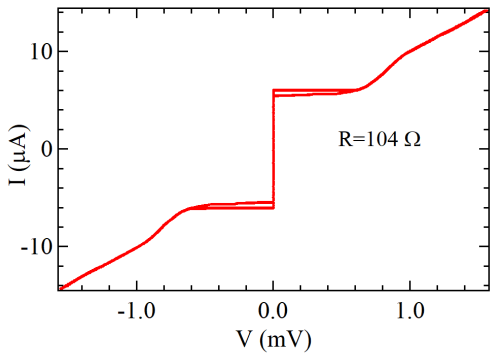

Figure 2.2. Current-Voltage characteristics (IVC) of the FHIB YBCO junction at 50 mK. The junction resistance $R = 104\,\Omega$ is obtained from the linear part of the IVC (|V|>1 mV). The retrapping current $I_r \approx 0.9 I_c$ yields $Q_0 \approx (4\pi I_c)/I_r \approx 1.4$.

We experimentally studied the T-dependence of $\langle I_s \rangle$ and σ between 50 mK and 3.0 K using the time-of-flight technique with a normalized bias current ramping rate $di/dt \equiv I_c^{-1} dI/dt = 1000/$ s. At each temperature 50,000 switching events were acquired to produce a smooth $P(I)$, as shown in FIG. 2.3(a). FIG. 2.3(b) shows the measured $P(I)$ in the temperature range of $3\,\mathrm{K} \leq T \leq 50\,\mathrm{mK}$ for junction JJ2 (Table 3.1). The different escape mechanisms are reflected in the characteristics of the measured SCDs: the mean $\langle I_s \rangle$, the standard deviation σ, and the skewness γ_3. The overlapping SCDs at $T < 0.8\,\mathrm{K}$, signify the occurrence of MQT. A progressive narrowing of $P(I)$ occurs when the temperature is increased beyond 0.8 K. The shape of the distribution changes gradually from asymmetric to symmetric as T increases, quantified by the measured skewness γ_3, as shown in the inset of FIG. 2.3(b). The behavior is similar for all of the junctions measured qualitatively despite having different classical to quantum crossover temperatures T_{cr}.

For $T < 0.8$ K the experimental data agree with the result of numerical calculation using the MQT rate equation Γ_q (Eq. (1.20)) with I_c and C as the only adjustable parameters while keeping the value of $R = 104\ \Omega$ and $I_c^{-1} dI/dt = 1000/\mathrm{s}$ constant. The best fit to $\langle I_s \rangle$ and σ at $T < 0.8$ K and the observed crossover temperature $T_{cr} = 0.8$ K yields $I_c = 7.55\,\mu\mathrm{A}$ and $C = 8.0\,\mathrm{fF}$, which is consistent with the result of FastCap simulation. At $T > 0.8$ K, the measured mean switching cur-

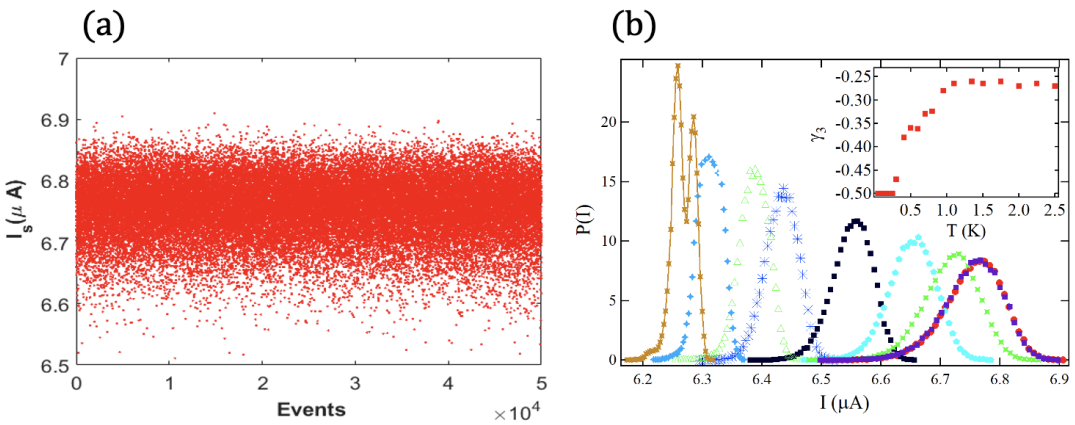

Figure 2.3. (a) The 50,000 switching events collected for a junction JJ2 at a particular T of 50 mK. (b) The measured switching current distribution (SCD) at different temperatures for a junction JJ2 having parameters reported in Table 3.1. From right to left are the SCDs taken at 50 mK to 3 K. For the shake of clarity, only a few selected SCD's are shown. Below 0.8 K the SCD's overlap and only one distribution have been shown. Inset shows the skewness, γ_3 of the SCDs. The SCDs in the MQT regime are negatively skewed with a constant value of ~ -0.5. During the transition from MQT to PD, the SCDs skew gradually decreases with the rise in T and remains constant ~ -0.27 for higher temperature SCDs.

rent increasingly deviates from the mean escape current $\langle I_{\rm esc}\rangle$ of thermal activation computed from $\Gamma_{\rm TA}$ (Eq. (1.19)) due to phase diffusion (PD) which is caused by frequent retrapping of the phase particle after it escapes from metastable potential wells [114, 115]. In the case of PD, switching to the running state occurs at a bias current $\langle I_s^{PD}\rangle$ that is higher than the value computed from Eq. (1.19). At the same time, σ becomes increasingly narrower than if PD was absent. The most distinctive fingerprint of PD is $d\sigma/dT < 0$, which is in stark contrast to $d\sigma/dT > 0$ of TA without PD as shown in FIG. 2.4. Furthermore, as T increases, the skewness, γ_3, becomes less negative and ultimately goes to zero when PD is prevalent [52, 53]. All of these distinctive features of PD have been observed in our experiment.

In FIG. 2.4(b) saturation of $\sigma(T)$ at $T < T_{\rm cr}$ is observed, which is the most substantial evidence of MQT, provided it is not caused by extrinsic current noise in the measurement circuit and joule

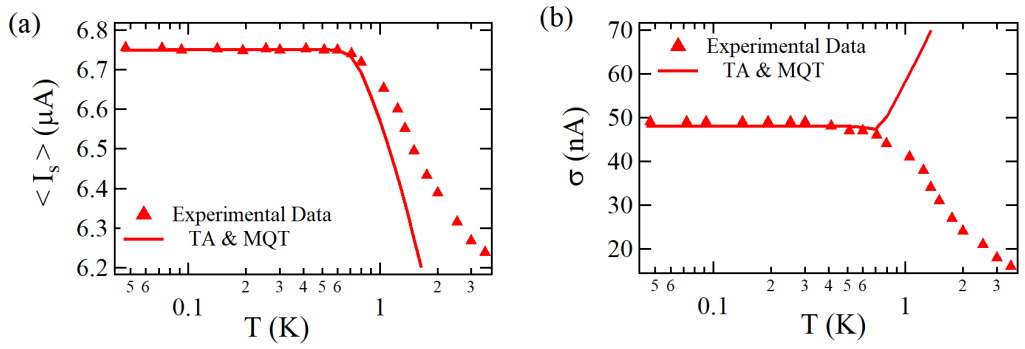

Figure 2.4. The temperature dependence of (a) the mean $\langle I_s \rangle$ and (b) the width σ of switching current distributions. The triangles are experimental data and the solid lines are the theoretical prediction of MQT (TA), assuming no phase diffusion.

heating. The possibility of extrinsic current noise can be ruled out by the much narrower width (less than one-half of the width at low T) of the data in the phase diffusion regime. To determine if the saturation below 0.8 K was due to Joule heating, we inserted an idle time, during which $I = 0$, of variable length between successive current sweeps. We found no changes in the measured mean and width as the idle time was varied from about 50 μs to 50 ms, excluding joule heating as the cause of low-temperature saturation of the mean and width. Furthermore, the solid line in FIG. 2.4(b) was calculated from the MQT model with the same set of parameters used for the solid curve in FIG. 2.4(a). Therefore, we conclude that the observed low T saturation of mean and width provides unambiguous evidence for MQT in the planar Y-Ba-Cu-O Josephson junction made by FHIB.

In summary, we observed unambiguous evidence of MQT in a moderately damped ($Q_0 \simeq 1.4$) planar Y-Ba-Cu-O nano Josephson junction made by FHIB direct-writing. The mean and width of the measured switching current distributions agree very well with the MQT theory below the quantum-to-classical crossover temperature $T_{cr} \approx 0.8$ K with junction's shunt capacitance C and the damping resistance R constrained by the results of FastCap simulation and the measured I-V characteristics. The result also shows that above 0.8 K phase diffusion played a significant role in the phase dynamics of this moderately damped junction. By varying the idle time from 50 μs to 50

ms we rule out the possibility of that the observed saturation of mean and width of SCD was due to heating. Furthermore, the observed saturation of width at $T < T_{cr}$ could not be due to current noise in the measurement circuit because σ at $T > 2$ K is much less than σ at $T < T_{cr}$. The experimental confirmation of MQT in FHIB planar Y-Ba-Cu-O Josephson junctions is the first step towards the realization of coherent quantum behaviour.

In FIG. 2.4(a) at $T > 0.8$ K, we observed the experimental $\langle I_{\rm s} \rangle$ deviates from the $\langle I_{\rm esc} \rangle$ computed from thermal activation (TA). In the next chapter, we try to address the cause behind the deviation and discuss the diffusive motion (PD) of the phase particle after the first escape.

Chapter 3

Phase diffusion in Josephson junctions

In this chapter, the phase particle's motion after escaping from the trapped state is investigated both experimentally and numerically. The result clarifies the critical role played by the tilt of the potential energy of the Josephson junction, which has been neglected in previous studies of PD.

3.1 Theory of phase diffusion in Josephson junctions

Brownian motion in a periodic potential constitutes one of the fundamental and general problems of particle transport with numerous applications in various fields of science and technology. Kramers first studied the noise-activated escape of a particle from a metastable potential well in different damping regimes [41]. His work provided a framework to understand diffusion's role in the dynamical behavior of many systems in science and engineering [116–119]. For example, the theory has been extended to study thermal ratchets as a possible model for molecular motor proteins [120, 121]. In physics, Josephson junctions have provided excellent testbeds to study escape dynamics in the tilted washboard potential [36, 115, 122–124]. Because of the design flexibility and controllability, JJ is used to study the nature of the interaction between the quantum system and the environment. Also, it has served as a platform to compare different theoretical predictions with experimental data to reveal possible new physics in the tilted periodic potential systems

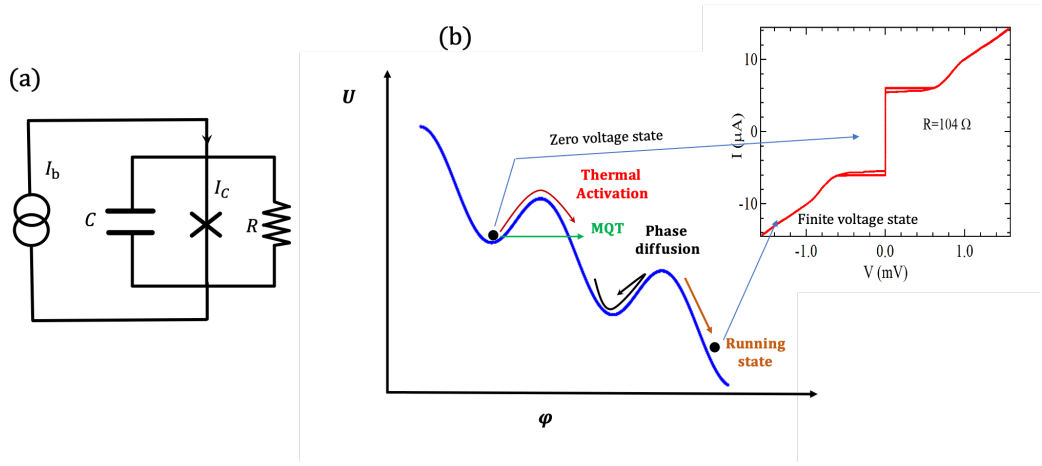

Figure 3.1. (a) The equivalent circuit diagram of a Josephson junction according to the RCSJ model in which R is the effective frequency-independent resistance. (b) The phase dynamics of a current biased Josephson junction and the measured I-V characteristic. In the superconducting state (zero voltage state), the fictitious phase particle is trapped in one of the metastable potential wells, where it oscillates back and forth near the bottom of the well thus the average voltage is zero. The phase particle can escape from the potential well either by thermal activation (TA) or macroscopic quantum tunneling (MQT). Depending on the tilt of the potential controlled by the bias current and the damping strength characterized by Q_0, there is a finite probability of the phase particle being retrapped in one of the subsequent wells before the system switches to the running state. Repeated escape and retrapping in subsequent potential wells gives rise to the diffusive motion of the phase particle called phase diffusion (PD).

[42, 51, 125]. In addition, depending on junction parameters and characteristics of quantum and thermal fluctuations, different regimes such as TA, MQT, PD, and quantum phase diffusion, QPD can be thoroughly investigated [52, 53, 77, 126]. Thus, it is essential to understand the governing factors behind the different escape dynamics and subsequent motion of Josephson junctions.

As explained in section 1.3, phase dynamics of a current biased Josephson junction is equivalent to a fictitious phase particle of mass C moving in the tilted washboard potential $U(\varphi)$ described by Eq. (1.15). The main factors governing the dynamics of the phase particle are the bias current, which controls the tilt of the potential, damping strength characterized by the quality factor Q_0, the

thermal (quantum) fluctuations originating from the effective resistance R of the junction, and E_J and E_C parameters of the junction [49, 127]. The role of each factor played in the dynamics of the phase particle is discussed below.

In the absence of a bias current, the tilt i of the washboard potential is zero and ΔU is maximum. The phase particle oscillates at the bottom of a metastable potential well with plasma frequency ω_{p0}. In this case, the time average of $\varphi(t)$ is zero. In the presence of a bias current of $I < I_c$ (i.e., $i < 1$), the washboard potential is tilted reducing barrier height and plasma frequency. For $i \geq 1$, the potential has no minima, and the particle rolls down the potential landscape with a finite velocity, $\dot{\varphi}$. This situation corresponds to the case in which the junction switches out of its dissipationless zero-voltage state to the finite voltage $V = (\hbar/2e)\dot{\varphi}$ state. Thus, the tilt i plays a major role in the phase particle's motion in the washboard potential.

Damping also plays an important role in the dynamics of the phase particle. The strength of damping is measured by the quality factor $Q_0 = \omega_p RC$. However, the source of damping in Josephson junctions remains unsettled [126, 128]. Different authors have presented their views about what determines the effective resistance R. Kautz and Martinis [47] have reported phase diffusion in small hysteretic Josephson junctions ($I_c \sim$ nA) and E_J comparable to thermal energy $k_B T$. They concluded that the high-frequency impedance of the circuitry is the cause of damping. Similarly, Martinis *et al.* demonstrated through a detailed measurement that the frequency-dependent dissipation $\mathrm{Re}[Z(\omega_p)]$ rather than the subgap quasi-particle resistance of the junction is responsible for damping [125]. Washburn *et al.* has studied the effect of dissipation and temperature on MQT rate and found that instead of the subgap quasi-particle resistance R_{qp}, normal resistance R correctly predicts the MQT rate and the cross-over temperature (T_{cr}) [70, 71]. In our case, the Y-Ba-Cu-O JJs measured typically have a normal resistance R considerably smaller than the free space impedance, $Z_0 = \sqrt{\mu_0/\varepsilon_0} \simeq 377\,\Omega$, and are well described by the RCSJ model with frequency-independent Q_0 [115, 125, 129].

In reality, the experiments are conducted at $T > 0$ so that the effective damping resistance R exhibits Johnson-Nyquist noise [47, 130]. The noise has physical consequences on the dynamics of the Josephson junction. In the presence of thermal fluctuations, the phase particle might escape from the potential well and then run-down the washboard potential even at $i < 1$. In other words, thermal fluctuations could cause premature switching of the junction to the finite voltage state. It also plays an important role in the retrapping of the phase particle after the initial escape [51, 72].

Furthermore, as $T \to 0$, thermal noise is dominated by the zero-point current fluctuations (quantum fluctuation) in the shunt resistor, causing dissipation in the MQT regime [131]. The rate by which the phase particle escapes from the metastable potential well due to thermal activation (TA) depends on temperature (section 1.4.1). After the initial escape, there is a finite probability of the phase particle being retrapped in one of the subsequent potential wells depending on the strength of the damping Q_0 and the tilt of the potential i. At low current bias, the process of escape and retrapping may occur multiple times, which generates diffusive motion of the phase particle. As the bias current is ramped up, the potential's tilt increases and the phase particle's velocity rises, which ultimately leads to a switch to the running state. The competition between multiple escapes and retrapping prevents the junctions from entering the running state. It leads to the appearance of a tiny non-zero voltage, manifesting as a phase diffusion branch in the I-V characteristic [47, 49]. Thus, the dynamics of the phase particle crucially depend on three metrics: the tilt (i) of the potential, the strength of damping, and thermal (quantum) fluctuations. The interplay between these factors determines the occurrence of various phenomena, MQT, TA, and PD in the phase dynamics of Josephson junctions.

In our experiment, we measured the SCD's of planar Y-Ba-Cu-O nano Josephson junctions and observed clear evidence of direct transition from MQT triggered escape followed by PD regime. Here, we are interested in understanding the physics of PD regime. Although we are not the

first to observe transition from MQT to PD in Josephson junctions our result sheds new light on an outstanding issue which has not been correctly identified in previous studies. Several authors to understand of PD by proposing a phase diagram in terms of the ration E_J/E_c and k_BT/E_J [80, 129, 132, 133].

The various regimes of Josephson junction's phase dynamics can be classified by constructing a phase diagram [49, 134]. L. Longobardi *et al.* has observed a direct transition from MQT triggered escape to PD regime in Y-Ba-Cu-O biepitaxial Josephson junctions [77]. They performed numerical simulations to determine the transition curve between the PD and the running state, and the various regimes are explored by spanning the parameter space (k_BT/E_J, Q_0). As discussed above, tilt i also plays an important role in Josephson junction's phase dynamics along with Q_0 and T. However, the phase diagram they simulated did not consider the effect of tilt i.

3.2 Numerical simulation of retrapping probability

Based on the RCSJ model of Josephson junction and the second Josephson relation $\hbar\omega_p = 2eV$, the equation of motion of a current biased Josephson junction in the presence of thermal fluctuations is [42]

$$C\Big(\frac{\Phi_0}{2\pi}\Big)^2\ddot{\varphi} + \frac{1}{R}\Big(\frac{\Phi_0}{2\pi}\Big)^2\dot{\varphi} = -\frac{\partial U(\varphi)}{\partial\varphi} + \Big(\frac{\Phi_0}{2\pi}\Big)I_n(t). \tag{3.1}$$

The shunt resistance, as shown in FIG. 3.1(a) is the source of current fluctuations at finite temperatures. The noise current $I_{\rm n}$ is originated from the Johnson noise of the shunt resistance. The statistical properties of this noise current, according to the fluctuation-dissipation theorem [135] is

$$\langle I_n(t)\rangle = 0 \tag{3.2a}$$

$$\langle I_n(t) I_n(t')\rangle = \frac{2k_B T}{R}\delta(t-t') \tag{3.2b}$$

The dimensionless form of Eq. (3.1), which has the advantage of reducing the number of system parameters can be obtained by normalizing current to I_c, and time to ω_{p0}^{-1}

$$\ddot{\varphi} + G\dot{\varphi} = -\sin\varphi + i + i_n(\tau), \tag{3.3}$$

where $G = 1/Q_0$, and $\tau = \omega_{p0}t$. Here, single and double overdot on φ represent the first and second derivative with respect to, τ. A finite difference technique [42, 136] is implemented to propagate Eq. (3.3) with accuracy of $O(\delta\tau^3)$, where the time step $\delta\tau = 2\pi/250$ is determined through a convergence test. In a convergence test, $\delta\tau$ is decreased until the result of the simulation does not change anymore. The time step at which the result becomes stable is chosen for the simulation.

$$\varphi_{n+1} = 2\varphi_n - \varphi_{n-1} - G(\varphi_n - \varphi_{n-1})\delta\tau + (i - \sin\varphi_n + \varepsilon q_n)\delta\tau^2, \tag{3.4}$$

where $\tau_{\rm n} = {\rm n}\,\delta\tau$, $\varphi_{\rm n} \equiv \varphi(\tau_{\rm n})$, $\varepsilon = \sqrt{2Gk_{\rm B}T/E_{\rm J}\delta\tau}$, and $q_{\rm n}$ is a Gaussian random process with the standard normal distribution: $\langle q_{\rm n}\rangle = 0$ and $\langle q_{\rm n} q_{\rm m}\rangle = \delta_{\rm nm}$.

The washboard potential has a local minima located at $\varphi_{\rm min} = \sin^{-1} i$ and maxima at $\varphi_{\rm max} = \pi - \sin^{-1} i$. The motion of the fictitious phase particle is tracked using Eq. (3.4). We start a simulation by initializing the fictitious phase particle at $\varphi_{\rm max}$ and release it with an initial forward velocity determined from the thermal equilibrium condition, $k_B T/2 = C\dot{\varphi}^2/2$. We track its trajectory as it moves in the washboard potential for 20 consecutive wells ($20 \times 2\pi$). The average time needed to transit directly to the running state (traverse 20 wells without hindrance) from one of the potential maxima depends on the T and the tilt i. For $T = 4\,{\rm K}$ and $i = 0.99$, it requires $\tau = 156$ on

average. Thus, in a trial, $\tau_{\text{limit}} < 251$ (to be on the safe side) is taken as the criteria to determine if the phase particle retrapping had occurred or not. For a given T and tilt i, we run the simulation for 10^4 trials to reduce statistical uncertainty. Let N_{run} be the number of times the phase particle directly transits to the running state from which probability of running, P_{run} is obtained. Finally, probability of retrapping is calculated as $P_{\text{retrap}} = 1 - P_{\text{run}}$.

3.3 Results and discussion

The temperature dependence of the mean $\langle I_s \rangle$ and width (σ) of the $P(I)$ for JJ1 and JJ2 are shown in FIG. 3.2. JJ1 and JJ2 show similar behavior of escape via MQT followed by PD. The shunt resistances, R of each junction is determined from the linear part of the I-V curve at $V \geq 1\,\text{mV}$. While the critical current, I_c and capacitance, C is determined by fitting the σ of the SCD's at $T < T_{\text{cr}}$. The key parameters of each junction are listed in Table 3.1. We are unable to fit the PD data due to a lack of well-established analytical results.

Sample	$I_c\,(\mu\text{A})$	$R\,(\Omega)$	$C\,(\text{fF})$	$T_{\text{cr}}\,(\text{K})$	$\omega_{p0}(\text{THz})$	Q_0	$E_J(\text{K})$	E_J/E_C
JJ1	16.0	60	8.0	0.5	2.47	1.20	381	3282
JJ2	7.55	104	8.0	0.7	1.70	1.41	180	1549

Table 3.1. Device parameters for the Y-Ba-Cu-O Josephson junctions measured.

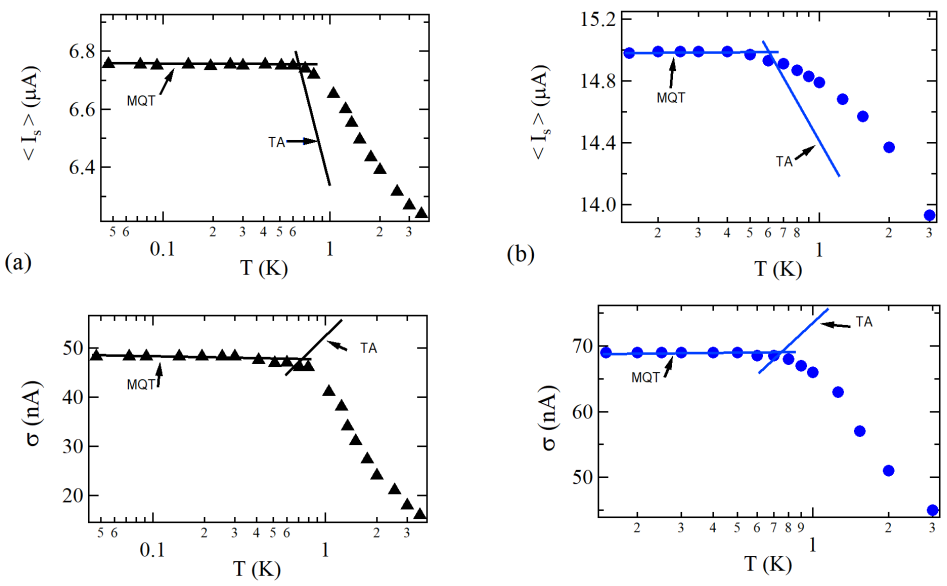

Figure 3.2. (a) and (b) shows temperature (T) dependence of the mean ($\langle I_s \rangle$) and the width (σ) of the SCD's for the measured junctions JJ1 (blue) and JJ2 (black) respectively. A transition from MQT to PD regime occurs at a temperature T_x. σ independent of T and negative $\partial\sigma/\partial T$ are the hallmark of the MQT and PD regime respectively. The junction parameters are determined from the theoretical fit (solid line) to the MQT regime data. The intersection between MQT and TA determines the cross-over temperature (T_{cr}).

The combination of junction parameters, leads to the occurrence of two distinct behaviors: switching to the running state with and without going through the intermediate state of PD, in moderately damped Y-Ba-Cu-O planar Josephson junctions. The data show that T_{cr} of the junctions is ~0.5-0.8 K reflecting the high characteristic plasma frequency ($\omega_{p0}/2\pi \sim$ THz) of the junctions. Since MQT has been discussed previously in chapter 2 we focus on understanding PD observed in these junctions. FIG. 3.3 shows the normalized mean switching current vs. temperature (normalized to E_J) of JJ1 and JJ2. The comparison between mean $\langle I_s \rangle / I_c$ of JJ1 and JJ2 show that the junction with larger E_J but nearly same ω_{p0} requires greater tilt to enter MQT regime. Consequently, the junction with smaller E_J has higher T_{cr}.

The probability of the phase particle being retrapped in subsequent potential wells as a function of T for different tilt values, i, is shown in FIG. 3.4. For each value of T, P_{retrap} is obtained by

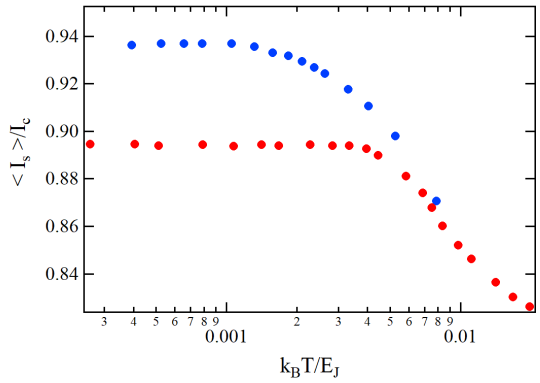

Figure 3.3. The normalized mean switching current, $\langle I_s \rangle / I_c$, as a function of $k_B T/E_J$ for junctions JJ1 (blue) and JJ2 (red). The parameters determined from best-fit obtained for the junctions show that JJ1 has more than twice the value of E_J compare to JJ2. The tilt required to enter the MQT region for each junction is different. The larger junction (JJ1) requires greater tilt but smaller value of $k_B T/E_J$ to enter the quantum regime.

averaging over $10,000$ simulated retrapping events. For $i = 0.86$, P_{retrap} increases as T is increased and eventually reaches $P_{\text{max}} = 1$. The plot shows that, for a smaller tilt, the maximum retrapping probability is reached at a lower temperature. Even with reduced thermal fluctuations at a lower temperature, a smaller tilt increases the probability of retrepping of the phase particle.

We report the phase diagram by scanning the parameter space $(i, k_B T/E_J)$ as shown in FIG. 3.5 to summarize various escape mechanisms and to emphasize the importance of tilt in determining phase dynamics of the junctions. The phase diagram is obtained from the numerical simulation discussed in section 3.2 and calculation using TA and MQT rate Eqs. 1.19 and 1.20. The color bar shows the probability of being retrapped after escaping via MQT or TA from the initial potential well. At constant $k_B T/E_J$, P_{retrap} is an increasing function of tilt. Between the region no PD (blue) and severe PD (yellow) there is an intermediate transition region, where the particle can either escape or be retrapped while running down the washboard potential. In FIG. 3.5 red curves are the normalized mean escape current $\langle I_{\text{esc}} \rangle$ due to TA and MQT computed from Γ_{TA} and Γ_{q} for JJ1 and JJ2. At $T > T_{cr}$, the mean escape current due to TA takes place at a smaller tilt and falls into the

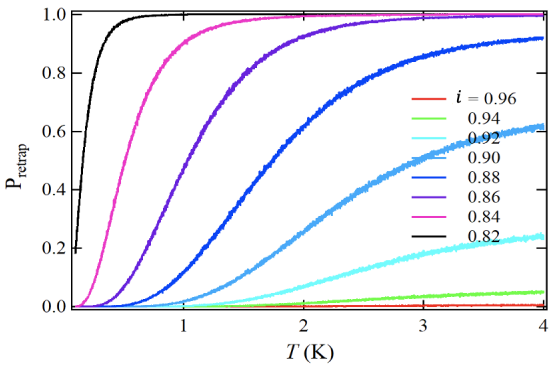

Figure 3.4. Result of numerical simulation: The temperature dependence of the retrapping probability, P_{retrap}, of the fictitious phase particle in subsequent potential wells. P_{retrap} for different tilt, i, of JJ2. The tilt is one of the determining factors of the retrapping probability.

region where P_{retrap} is high. The superimposed plot shows that after the initial TA-caused escapes, the phase particle undergoes frequent retrapping giving rise to TA-dominated PD. The magenta curves are obtained by doubling the value of I_{c} and C while reducing R to half, while the black curve is obtained by increasing I_{c} and C while decreasing R five-fold that of the red curve. In doing so, E_J (E_c) is increased (decreased) in proportion, while the quality factor Q_0 remains the same. The comparison shows that as E_J/E_c is increased, it requires a greater tilt, i, and smaller $k_{\text{B}}T/E_J$ to enter the MQT regime. Therefore, under the condition of same ω_{p0} and Q_0 junctions with smaller E_J/E_C have greater T_{cr}.

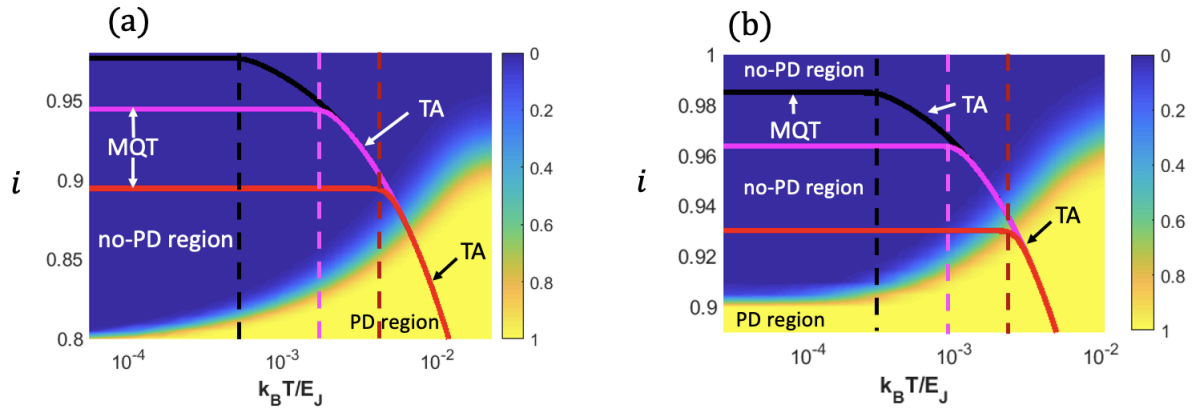

Figure 3.5. $(i, k_B T/E_J)$ parameter space, showing different escape regimes for JJ1 (b) and JJ2 (a). The color bar shows the probability of the phase particle being re-trapped in one of the subsequent potential wells. The red curve is the normalized mean escape current $\langle I_{esc} \rangle$ due to TA and MQT computed from Γ_{TA} and Γ_q for JJ2 and JJ1. The magenta curve is obtained by doubling the value of I_c and C while reducing R to half, whereas the black curve is obtained by a five-fold increase in I_c and C while decreasing R five-fold that of the red curve. The dash lines in the plot guide the location of MQT-to-TA crossover temperature, T_{cr} respectively.

In summary, we observed a transition from MQT triggered running state to PD regime. After the initial TA escape from the metastable well, the phase particle undergoes severe retrapping in subsequent potential wells before finally switching to the running state. The junctions investigated have comparatively small (small capacitance and low critical current junctions) Josephson coupling energy E_J and are in the moderately damped regime. Thermal fluctuations lead to premature switching, and for coincidentally $T > T_{cr}$ retrapping is significant at low bias current. Also, the experimental data and the phase diagram obtained from numerical simulation (FIG. 3.5) confirms that the tilt plays a crucial role in the phase dynamics of JJs. Junctions with larger E_J, but otherwise having the same ω_{p0} and Q_0, require greater tilt to transit to MQT from TA and/or the PD regime. Hence, the role of PD is to delay switching to the final running state which results in higher switching currents in the presence of PD.

Chapter 4

SQUID as fast Szilard engine

In this chapter, we investigate using SQUID based flux logic device to realize an efficient Szilard engine by numerical and experiment. Our results show that while the maximum work per engine cycle is obtained in the quasi-static regime the maximum power is achieved when the engine is run at a much faster speed.

4.1 Maxwell's demon thought experiment

In 1867, James Clerk Maxwell conceived a thought experiment known as Maxwell's Demon to challenge the Second Law of Thermodynamics [137, 138]. He imagined that an intelligent observer (demon) could decrease the entropy S of the system by separating the fast-moving and slow-moving molecules into two chambers [139, 140]. The two chambers then would contain gases with different temperatures, and that temperature difference may be used to power a heat engine to produce mechanical work in an apparent violation of the second law of thermodynamics [138, 141].

In 1929, Leo Szilard visualized the Maxwell's demon experiment with a single particle in a box in contact with a single heat bath operating in a cyclic fashion. This so-called "Szilard engine" can

thus convert heat completely into work, which seems to violate the Second Law of thermodynamics. Szilard found that the average amount of work that can be delivered by his engine per cycle is $k_{\mathrm{B}}T\ln 2$ [137]. Later in 1961, Rolf Landauer argued that to determine the position and speed of each molecule, the demon must store information about the state of the molecules [142]. In order to complete the thermodynamic cycle, the demon's memory needs to be erased, which is a thermodynamically irreversible process that costs energy. Landauer showed that the fundamental energy cost to erase one bit of information from the demon's memory is equivalent to the amount of the work extracted, $W = k_{\mathrm{B}}T\ln 2$, per cycle which rescued the Second Law of thermodynamics [143]. Landauer's erasure principle laid one of the bedrocks of information theory. Any logically irreversible operation, such as AND or OR has a fundamental minimum energy cost because the loss (erasure) of information.

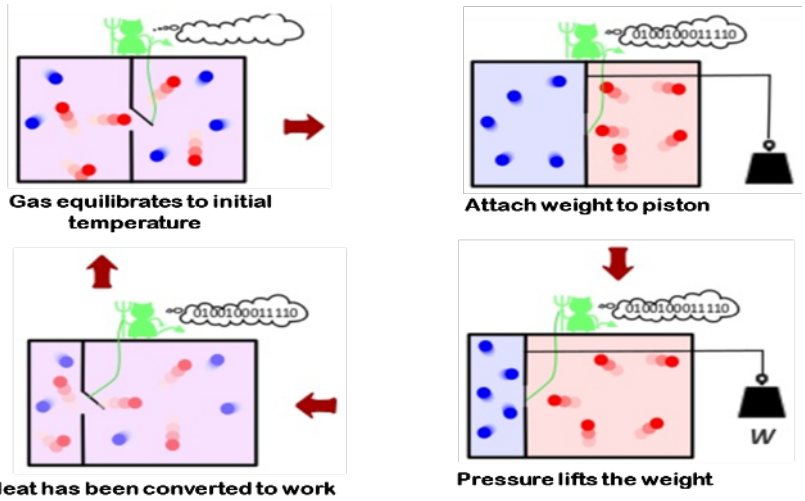

Figure 4.1. A Szilard engine working in a cycle. The amount of work extracted by the engine from the heat bath in one cycle should, in fact, be equal to the energy needed to erase information from the demon's memory.

For over a century, much effort has been devoted to confirm the link between information and thermodynamics and to determine experimentally the energy cost of manipulating information

[144–147]. In past decades, there has been a significant theoretical and experimental progress in extending stochastic thermodynamics and fluctuation theorems into nano-systems [141, 148–153]. Due to the technological advancement, the study of energy fluctuations in nano-scale systems such as optical or electrical traps [144, 146, 154] and single-electron tunneling (SET) devices [143, 155] has transformed the thought experiments such as the Maxwell's demon and the Szilard's engine to experimental realizations.

Recently, Koski et al. [145] demonstrated a Szilard engine using a single electron box that showed the extraction of $k_{\mathrm{B}}T\ln 2$ of heat by creating a bit of information. They showed that it is possible to create a heat engine with only a single thermal reservoir, which apparently violates the Second Law of thermodynamics [156]. Single-electron tunneling (SET) device has thus paved a way to understand and design nano-engines with information as fuel [21, 157–159].

To improve the nano-device-based Szilard engine's performance, it is imperative to understand factors that are critical to Szilard engine's performance [160]. The understanding will provide insights into the optimization of nano-motors and devices driven by thermal fluctuations [161]. Furthermore, studies may provide a basis to extend the stochastic thermodynamics into the quantum regime where quantum heat engines may perform better than their classical counterparts [162–164].

However, heat engines realized through single-electron circuits have limitations in terms of power performance, which is the amount of work done by converting heat extracted from the heat bath per unit time [157]. The SET-based Szilard engines and the bit erasure protocols realized in experiments operated in the frequency range of 10-10^3 Hz [165], making them slow to convert heat into work. For example, the typical slow ramp time of SET-based devices is on the orders of $\sim 10^{-3}$-1 s [145], which severely limits their performance in terms of the power output.

In this work, we propose a much faster Szilard engine using a superconducting quantum interference device (SQUID) that functions as a flux logic device (FLD) under appropriate conditions. The flux logic device has a single degree of freedom denoted by the dynamical variable Φ, which is the total magnetic flux threading the loop, as shown in FIG. 1.8. The device has a one-dimensional (1D) double-well potential separated by a barrier, as shown in FIG. 4.2. An externally applied flux Φ_x sets the tilt, ε, of the potential. Thus, in the classical regime, the system's behavior is equivalent to a fictitious flux particle moving in the 1D double-well potential in contact with a single heat bath of temperature T. In the following we demonstrate that SQUID functions excellently as a flux logic device and that SQUID-based logic device is an ideal prototype for constructing Szilard engines with unprecedented speed and power through numerical simulation. The double-well potential can be treated as a one-bit memory having two discrete states, "-1" and "1" corresponding to the flux particle in the left and right well, respectively. We first show that in the quasi-static (QS) limit, on average, the proposed heat engine can extract $k_{\mathrm{B}}T\ln 2$ of heat per cycle from the thermal reservoir per bit of information created. Second, we found that the maximum power delivered by such a Szilard engine is not achieved by operating it in the quasi-static limit but in a region far away from the QS limit. For most applications, a heat engine that can run fast and deliver greater power is more desirable than an engine that maximizes the average work done per cycle by going quasi-static (i.e., slowly) which results in diminishing output power.

4.2 SQUID-based flux logic device

As discussed in section 1.5, dynamics of SQUID-based flux logic device is analogue to a particle of mass 'C' moving in a potential given by Eq. (1.24). Based on the RCSJ model, the deterministic equation of motion of the flux logic device is given by Eq. (4.9). Eq. (4.9) describes the dynamics of the flux logic device moving in a 1D potential $U(\Phi)$ given by Eq. (1.24) with a damping coefficient R^{-1} [166]. Two parameters β_L and ϕ_x determine the shape of the double well potential (section 1.5). When $\phi_x = 1/2$ and $1 < \beta_L \lesssim 4.6$ the potential is symmetric about $\phi = 1/2$ with two

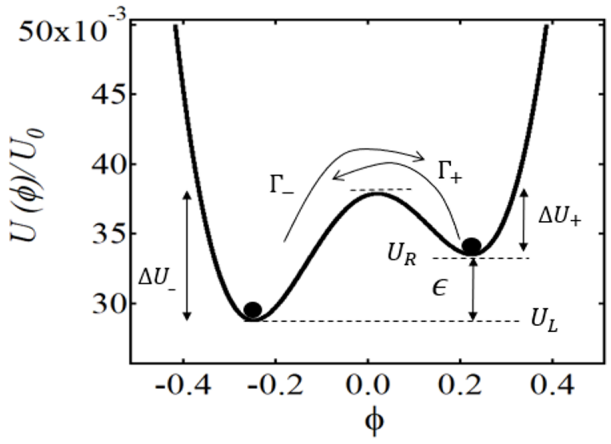

Figure 4.2. The potential of the flux logic device (FLD) at normalized external flux ϕ_x= -0.49 with $\beta_L = 1.49$. $\varepsilon \equiv \Delta U_+ - \Delta U_-$ is the energy difference between the two potential minima, where $\Delta U_\pm$ are the energy difference between the saddle point and the respective potential minima. $\Gamma_\pm$ is the escape rate out of the right and the left potential wells.

wells separated by a potential barrier ΔU_0. Changing ϕ_x slightly away from $1/2$ tilts the potential which results in an energy bias $\varepsilon \equiv U_R - U_L \equiv \Delta U_+ - \Delta U_- \propto \delta\phi_x \equiv \phi_x - 1/2$ between states "-1" (left well) and "1" (right well), where $\Delta U_\pm$ is the barrier height of the left and right well as shown in FIG. 4.2.

4.3 Experiment

4.3.1 Lifetime measurement

The FLD has two well-defined fluxoid states, current circulating clockwise as "-1" and current circulating anticlockwise as "1". In the classical regime, if the logic device is prepared in the "-1" state at $t = 0$, the probability of finding the logic device remaining in the same state at a later time is

$$P_s(t) = e^{-t/\tau}, \tag{4.1}$$

where $\tau = \Gamma^{-1}$ is the lifetime of the state under consideration. Γ is the escape rate by thermal activation which is given by Arrhenius law [57], and the escape rate from "-1" state to "1" state, and vice-versa is given by

$$\Gamma_{\pm} = a_t(\omega_p/2\pi)\exp(-\Delta U_{\pm}/k_B T). \tag{4.2}$$

In Eq. (4.2), the exponential term is the Maxwell Boltzmann probability that the particle will have energy equal to $\Delta U_{\pm}$ and escape to the other state while the term $\omega_p/2\pi$ is the attempt frequency. The dimensionless damping dependent factor, $a_t \in (0,1)$, takes different forms depending on the strength of the damping. At $\phi_x = 1/2$, we have $\varepsilon = 0$ and $\Gamma_+ = \Gamma_- \equiv \Gamma_0$. The energy bias, ε, is the key parameter to calculate various thermodynamic quantities.

SQUID based flux logic device we used has two superconducting loops. First, the main loop of inductance L with ϕ_x the external flux threading the loop. Second, the dc SQUID loop of inductance L_{dc} with $\phi_{x,dc}$ the external flux threading it. ϕ_x controls the tilt (ε) of the double-well potential while $\phi_{x,dc}$ tunes the barrier height as explained in Eq. (1.25).

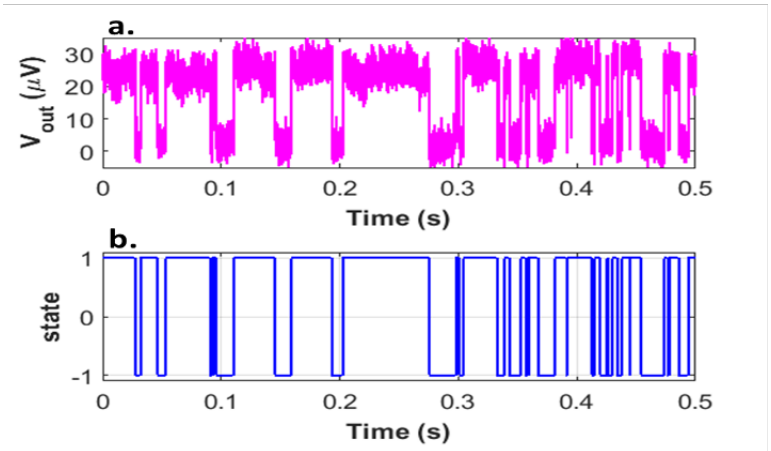

Figure 4.3. The magnetometer is operated at the most sensitive region so that it can clearly distinguish the two fluxoid states of the logic device (a) and the raw signal is digitized using a MATLAB code where state "± 1" represents the distinct fluxoid state of the logic device (b).

In the experiment, the average time the system remains in a given state depends on the barrier

height, which is controlled by $\phi_{x,dc}$ and the tilt ε which in turn is proportional to ϕ_x. We choose a suitable $\phi_{x,dc} = 0.29$ ($\beta_L = 1.49$), which is determined from calibrated voltage-to-flux relation $\phi_{x,dc} = (V_{x,dc} - V_{ref})/V_{dc,0}$, where $V_{dc,0} = 15.0\,\mathrm{V}$ corresponds to one flux quantum in dc SQUID loop while $V_{ref} = -0.8\,\mathrm{V}$ corresponds to $\phi_{x,dc} = 0$. When $\phi_x = 1/2$, the logic device's potential is symmetric, and the lifetime of the two states is same. For $\phi_x \neq 1/2$, the potential of the system is tilted, and the transition rates are given by Eq. (4.2). In order to determine the lifetime at specific $\phi_{x,dc}$ and ε, the system is allowed to thermalize for a time $t >> \tau$, and the flux in the main loop is monitored continuously by a dc SQUID magnetometer inductively coupled to the main loop.

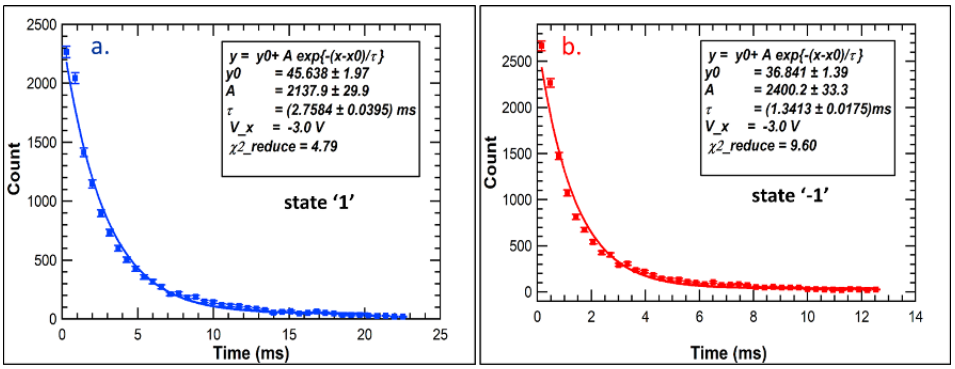

Figure 4.4. Histogram to get the lifetime of the state for a particular external main loop voltage, $V_x = -3.0\,\mathrm{V}$, and dc voltage, $V_{x,dc} = -5.1\,\mathrm{V}$. The time fictitious flux particle spends in the state "1" is $\tau_+ = (2.76 \pm 0.04)\,\mathrm{ms}$ while $\tau_- = (1.34 \pm 0.02)\,\mathrm{ms}$.

The time series of the magnetometer's voltage $V(t)$ is shown in FIG. 4.3(a). FIG. 4.3(b) shows the digitized form of $V(t)$ corresponding to flux logic device (FLD) in either "-1" or "1" state. The time the FLD remains in each state is then binned to form histograms. The exponential fits to histograms (see FIG. 4.4) yield each state's lifetime at that $\phi_{x,dc}$ and ϕ_x. At temperature T, based on detailed balance, energy bias ε is related to the transition rates $\Gamma_\pm$ as

$$\frac{\varepsilon}{k_B T} = \ln\left(\frac{\Gamma_-}{\Gamma_+}\right). \tag{4.3}$$

Eq. (4.3) is used to calibrate ϕ_x vs. V_x. The plot of ε as a function of V_x is linear as expected FIG. 4.5 . The relationship between V_x and ϕ_x is given by

$$\phi_x = (V_x - V_{xsym})/V_0, \tag{4.4}$$

where $V_{xsym} = -3.02\,\mathrm{V}$ and $V_0 = 8.1\,\mathrm{V}$.

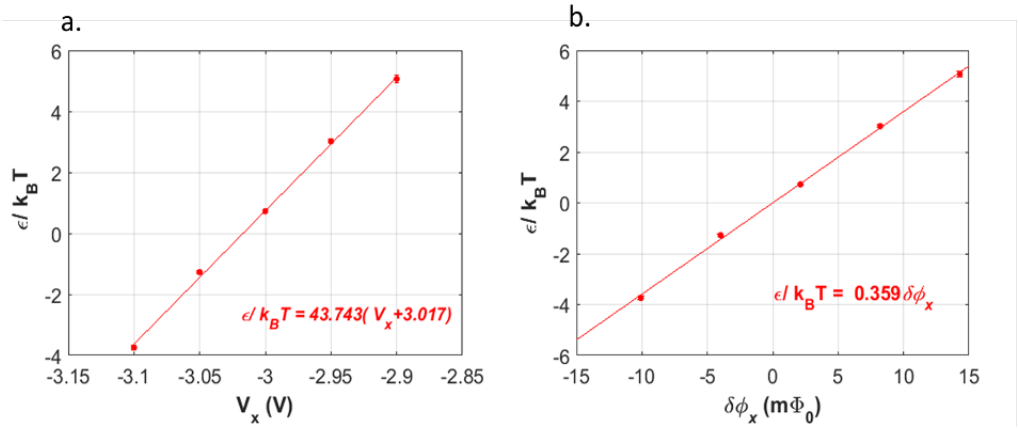

Figure 4.5. Energy bias as a function of V_x. The energy bias is zero at $V_x = V_{xsym} = -3.02\,\mathrm{V}$ (a) and the energy bias as a function of $\delta\phi_x = \phi_x - 1/2$.

4.3.2 Post selection method

In our experiment, a Szilard engine cycle consists of three stages: (i) slow ramp, (ii) measurement, and (iii) fast ramp. In the slow ramp stage, the system has a finite probability of jumping between two potential wells. During the time interval of $\delta t = t_{i+1} - t_i$, the change in energy bias $\delta\varepsilon = \varepsilon_{i+1} - \varepsilon_i$ increases. Since ε increases during the slow ramp, more heat is absorbed than released on one round trip of the particle. Here one round trip refers to the particle jumping from state "-1" (the left well) to state "1" (the right well) and subsequently returning back to the same state. In the measurement stage (ii), $\varepsilon = 0$, the net heat absorbed or released is always zero. The endpoint of the measurement stage is taken as the feedback point for the post-selection method. During the fast ramp stage (iii) of the successful cycles, there is no chance for the particle to jump

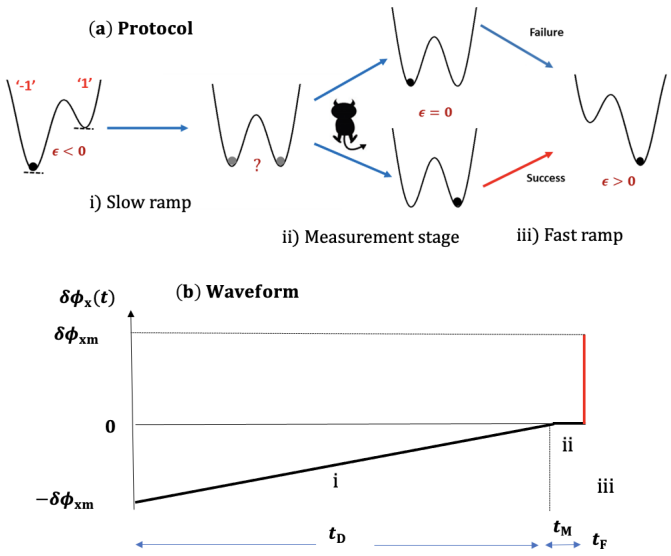

Figure 4.6. The post-selection protocol for Szilard engine experiment.

to state "-1", so there is no heat exchange between the FLD and the bath. Theoretically, the average heat absorbed $\langle Q \rangle$ should be $k_B T \ln 2$ per successful cycle when the slow ramp approaches the quasi-static limit. The detailed description of the thermodynamics of the engine in each stage is discussed in section 4.4.1.

The purpose of the experiment is to verify that in QS limit on average each successful cycle converts $\langle Q \rangle = k_B T \ln 2$ into work. In order to perform the Szilard engine experiment, we need to know Γ at $\delta\phi_x = 0$. The experiment is performed at $\phi_{x,dc} = 0.29$ for which $\Gamma^{-1}_{(\delta\phi_x=0)} = 3.0\,\text{ms}$. To circumvent the finite response time of in-situ feedback, we use the post-selection method to select only the successful cycles to analyze. Based on the state of FLD just before the fast ramp begins each cycle is assigned either as a "success" or a "failure". The data are analyzed after rejecting all failed cycles. Using post selection instead of real time feedback greatly simplifies the control and measurement circuits without compromising the validity of the result. The time for each cycle of operation is 200 ms. In our experiment, each cycle is started by initializing the FLD in the fluxoid state "-1". $\delta\phi_x$ is then ramped from $\delta\phi_x = -98.8\,\text{m}\Phi_0$ ($V_x = -3.8\,\text{V}$) to $\delta\phi_x = 0$ ($V_x = -3\,\text{V}$) in the slow ramp stage. The time for slow ramp stage is 128 ms which is much greater than the life

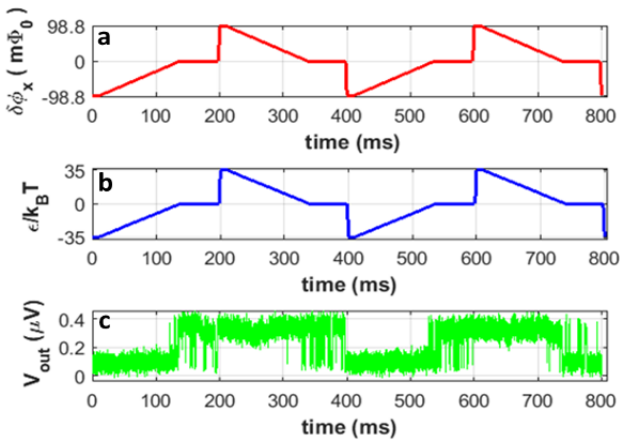

Figure 4.7. (a) The flux bias which drives the engine for Szilard engine experiment. The time period for each cycle is 200 ms while the lifetime at $\varepsilon = 0$ is 3 ms. (b) The control parameter ε converted using linear relation $\varepsilon/k_BT = 0.359\,\delta\phi_x$ as shown in FIG. 4.5(b). (c) The magnetometer's output voltage for the Szilard engine experiment.

time 3 ms to ensure sufficient time for thermalization. After reaching $\delta\phi_x = 0$, the FLD is thermalized for a time of 60 ms to reach thermal equilibrium. Finally, the FLD is driven by fast ramp for a 2 ms to return to $\delta\phi_x = 98.8\,\mathrm{m}\Phi_0$ corresponding to $\varepsilon_m = \varepsilon/k_BT = 35$ as shown in FIG. 4.7(b).

4.3.3 Heat absorbed and work done by the engine

The thermodynamics of each engine cycle is characterized quantitatively by the work done (W) by the engine and the heat absorbed (Q) from the thermal reservoir. For each leg of the cycle, W and Q are calculated from the instantaneous energy bias $\varepsilon(t)$, which depend linearly on the external flux bias $\delta\phi_x$ and the state of FLD. The accumulative work done by the engine and heat absorbed up to time τ_{i+1} is [58]

$$W_{i+1} = W_i + \frac{1}{2}F_{i+1}(\varepsilon_{i+1} - \varepsilon_i) \tag{4.5a}$$

$$Q_{i+1} = Q_i + \frac{1}{2}(F_{i+1} - F_i)\left(\frac{\varepsilon_{i+1} + \varepsilon_i}{2}\right), \tag{4.5b}$$

where $F_i = \pm 1$ is the discrete state variable of the SQUID, corresponding to the flux particle in the right (logic "1") or the left (logic "-1") potential well, at time τ_i. From τ_i to τ_{i+1}, the system absorbs or releases heat only if the particle jumped from one well to the other, which is calculated using Eq. (4.5b). The exact time at which the particle jumped is not important because when averaged over all jumps the middle point between τ_i and τ_{i+1}, i.e., $\tau_i + \delta\tau/2$ is an excellent approximation. In contrast, when the particle remains in the same state $F_{i+1} = F_i$, the work done by the engine from τ_i to τ_{i+1} is given by the second term on the right side of Eq. (4.5a). Using Eq. (4.5) it is straightforward to show that for each complete cycle, $W = Q$. The $\delta\phi_x(t)$ waveform depicted in FIG. 4.9 guarantees $W = Q \geq 0$ in agreement with the first law of thermodynamics [144].

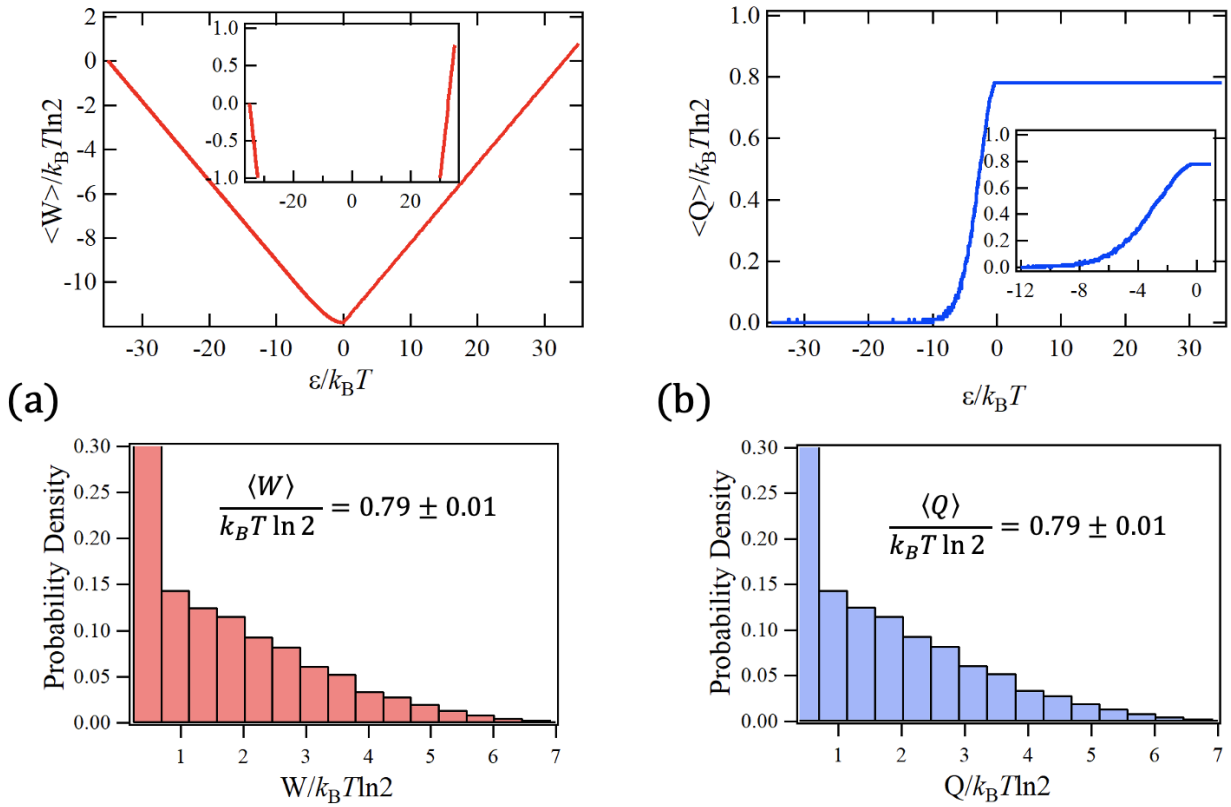

Figure 4.8. (a) Accumulative work done by the engine based on the average of about 26,000 successful cycles. Inset shows the zoomed in on (a) to show the average work done by the engine is positive. The corresponding distribution (red) of the work done by the engine averaged over successful cycles. (b) The accumulative heat absorbed by the engine averaged over 26,000 successful cycles and its corresponding distribution (blue). Inset: zoomed in for the slow ramp region. The slow ramp drive rate is $\dot{\varepsilon}/k_B T = 0.87\Gamma_0$ where $\Gamma_0 = 333\,\mathrm{s}^{-1}$ is the thermal activation rate when the potential is symmetric. The average heat absorbed by the engine per cycle is $\langle W \rangle / k_B T \ln 2 \cong (0.79 \pm 0.01)$, about 20 % less than that expected from Landauer's principle.

Our data show that for successful cycles the average work done by the engine per cycle is $\langle W \rangle / k_B T \ln 2 \cong (0.79 \pm 0.01)$, about 20 % less than that expected from Landauer's principle. For the slow ramp stage, ϕ_x is ramped from $\delta\phi_x = -98.8\,\mathrm{m}\Phi_0$ to $\delta\phi_x = 0$ (symmetric double well) linearly so that $\varepsilon(t) = -\varepsilon_m + \nu t$, where $\nu = d\varepsilon/dt$ is the ramp rate and $\varepsilon_m = 35$ (see FIG. 4.7(b)). The transition

rate from the left well (initial state) to the right well is

$$\begin{aligned}\Gamma(\varepsilon) &= a_t \frac{\omega_p}{2\pi} \exp\left(\frac{-\Delta U_-}{k_B T}\right) \\ &= a_t \frac{\omega_p}{2\pi} \exp\left[-B\left(\Delta U_0 - \frac{\varepsilon}{2}\right)\right] \\ &= \Gamma_0 \exp\left(\frac{B\varepsilon}{2}\right),\end{aligned} \tag{4.6}$$

where $\Delta U_\pm = \Delta U_0 \pm \varepsilon/2$ is the barrier height of the right well and the left well, ΔU_0 and the Γ_0 is the barrier height and transition rate when the potential is symmetric ($\varepsilon = 0$), respectively. $B = \beta = 1/k_B T$ for the thermal activation and $\kappa/\hbar\omega_p$ for quantum tunneling, where κ depends on the shape of the potential. For example, $\kappa = 36/5$ and $32/3$ for cubic potential and quadratic-plus-quartic potential, respectively. The probability of having a transition to occur between ε and $\varepsilon + d\varepsilon$ is denoted as $p(\varepsilon)d\varepsilon$, where the probability distribution function is

$$\begin{aligned}p(\varepsilon) &= \frac{\Gamma(\varepsilon)}{\nu} \exp\left[-\frac{1}{\nu}\int_{-\varepsilon_m}^{\varepsilon} \Gamma(\varepsilon')d\varepsilon'\right] \\ &= \frac{\Gamma_0}{\nu} \exp\left(\frac{B\varepsilon}{2}\right) \exp\left[-\frac{\Gamma_0}{\nu}\int_{-\varepsilon_m}^{\varepsilon} \exp\left(\frac{B\varepsilon'}{2}\right)d\varepsilon'\right] \\ &= \alpha B \exp\left(\frac{B\varepsilon}{2}\right) \exp\left[-2\alpha \exp\left(\frac{B\varepsilon}{2}\right)\right] \\ &= \alpha B \exp\left[\frac{B\varepsilon}{2} - 2\alpha \exp\left(\frac{B\varepsilon}{2}\right)\right]\end{aligned} \tag{4.7}$$

Assume $B\varepsilon_m >> 1$ so that $\exp(-B\varepsilon_m/2) \to 0$. In Eq. (4.7) $\alpha \equiv \Gamma_0/B\nu$ is a dimensionless constant. $\alpha >> 1$ leads to slow ramp and vice versa. Namely, α can be viewed as the key parameter that measures the goodness of adiabaticity. The accumulative probability that the particle escapes from the initial well when ramping from $-\varepsilon_m$ to $\varepsilon = 0$ is

$$P(0) = \int_{-\varepsilon_m}^{0} p(\varepsilon)\, d\varepsilon \;\; \simeq \int_{-\infty}^{0} p(\varepsilon)\, d\varepsilon = 1 - \exp(-2\alpha). \tag{4.8}$$

The experiment is performed at $\phi_{x,dc} = 0.29$ for which $\Gamma_0 = 333\,\mathrm{s}^{-1}$. The slow ramp drive rate is $\dot{\varepsilon}/k_BT = 0.87\Gamma_0$. Thus, the value of $\alpha \equiv \Gamma_0/B\nu = 1.22$ which gives $P = 91.3\,\%$, which signifies the slow ramp is not quasi-static enough to achieve Landauer's limit of $k_BT\ln 2$.

Our experiment is limited by a single slow ramp speed $\dot{\varepsilon}/k_BT = 0.87\Gamma_0$. To further our understanding of FLD Szilard engine we performed Monte-Carlo simulation to study the dependence of W on the ramp rate.

4.4 Numerical simulation of a fast Szilard engine

In the presence of thermal fluctuations, the dynamics of a SQUID is governed by the following Langevin equation

$$C\ddot{\Phi} + \frac{\dot{\Phi}}{R} = -\frac{\partial U}{\partial \Phi} + I_{\mathrm{n}}(t). \tag{4.9}$$

The shunt resistance R is the source of fluctuating current $I_{\mathrm{n}}(t)$. Eqs. (3.2a) and (3.2b) provide the statistical properties of this noise current, according to the fluctuation-dissipation theorem. Inserting the partial derivative of $U(\Phi)$ in Eq. (4.9) gives

$$C\ddot{\Phi} + \frac{\dot{\Phi}}{R} = \frac{\Delta\Phi}{L} - I_c \sin\left(2\pi\frac{\Phi}{\Phi_0}\right) + I_{\mathrm{n}}(t), \tag{4.10}$$

where, $\Delta\Phi = \Phi_x - \Phi$. Let $\varphi = \left(2\pi/\Phi_0\right)\Phi$ and time in normalized unit $\tau = \omega_{p0}t$. We have

$$\ddot{\varphi} + G\dot{\varphi} = \frac{\Delta\varphi}{\beta_L} - \sin\varphi + i_{\mathrm{n}}(\tau), \tag{4.11}$$

where $G = 1/Q_0$, $\Delta\varphi = \varphi_x - \varphi$. Eq. (4.11) is the dimensionless form of Eq. (4.9) which reveals universal behavior of the system. Here, single and double overdot in φ represents the first and second derivative with respect to time, τ. This stochastic second-order differential equation is simulated numerically using a finite difference technique [42, 136] with accuracy of $\mathrm{O}(\delta\tau^3)$, where

the time step $\delta\tau = 2\pi/250$ is determined through the convergence test:

$$\varphi_{n+1} = \left(2 - G\delta\tau - \frac{\delta\tau^2}{\beta_L}\right)\varphi_n - (G\delta\tau - 1)\,\varphi_{n-1} + \frac{\delta\tau^2}{\beta_L}\,\varphi_{x,n} - \sin(\varphi_n)\,\delta\tau^2 + \alpha\, q_n, \qquad (4.12)$$

where, $\tau_n = n\,\delta\tau$, $\varphi_{x,n} \equiv \varphi_x(\tau_n)$, $\varphi_n \equiv \varphi(\tau_n)$, $\alpha = \sqrt{2Gk_BT/E_J\delta\tau}$, and q_n is a random process with the standard normal distribution: $\langle q_n \rangle = 0$ and $\langle q_n q_m \rangle = \delta_{nm}$. For the sake of concreteness we performed simulation using a set of realistic device parameters listed in Table 4.1.

$I_c\,(\mu A)$	$L\,(pH)$	$C\,(fF)$	β_L	$\Delta U_0\,(K)$	$\omega_{p0}/2\pi\,(GHz)$
4.9	100	1200	1.49	20.3	18.0

Table 4.1. Flux logic device parameters

The simulation is performed for under-damped, moderately damped, and over-damped cases by setting the dimensionless damping factor, G= 0.1, 1, 3, and 10, respectively. The symmetric double-well transition rate, Γ_0 plays an important role in determining how fast the flux logic device can be operated as a Szilard engine. In this study, the transition rate Γ_0 for each damping parameter G, is found by propagating Eq. (4.12) at $\phi_x = 1/2$.

G	0.1	1.0	3.0	10
$\Gamma_0\,(10^7\,s^{-1})$	8.23	6.16	3.05	1.07

Table 4.2. Γ_0 for different values of G at T= 4.2 K.

We start the simulation by initializing the fictitious flux particle at the bottom of the left well and following its trajectory until it escapes into the right well. The time taken for each escape is recorded, and the procedure is repeated $50,0000$ times. The mean escape rate is obtained by averaging over all escape events for a given potential configuration and temperature. The values

of Γ_0 for different G at T = 4.2 K are listed in Table 4.2. The values of Γ_0 are in good agreement with Eq. (1.19).

4.4.1 Drive-measurement-feedback protocol

The drive-measurement-feedback protocol used to run the proposed fast Szilard engine is illustrated in FIG. 4.9 [167]. Each cycle of the Szilard engine consists of three stages: (i) creation of information, a slow ramp (drive) to extract heat from the bath, (ii) a measurement to determine the state of the flux logic device, and (iii) erasure of the information, a fast ramp to return the system to the same initial state without releasing heat back to the bath.

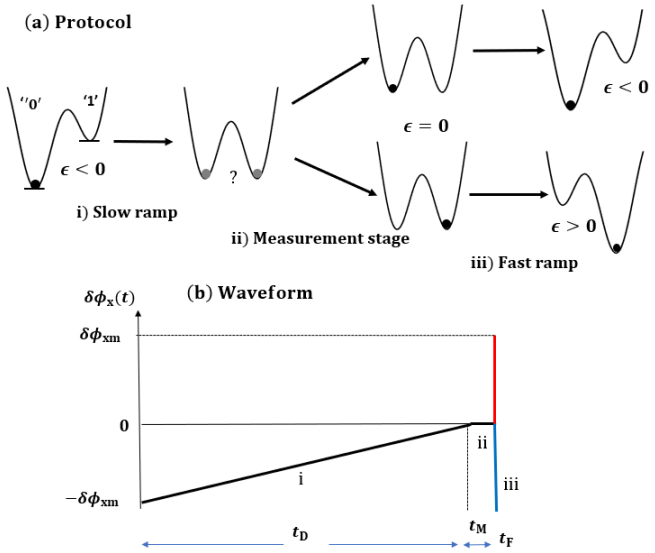

Figure 4.9. (a) Evolution of a flux logic device potential for a complete cycle. (b) Flux bias sequence as a function of time. Region (i) represents the slow drive for a time of t_D, the device is prepared for the measurement for a time t_M (ii), and the fast drive for a time t_F (iii). Depending on the outcome of the measurement, the end point of the cycle is either the same or the mirror image of the initial potential configuration due to its symmetric nature. Thus, the total cycle time is $t_{cycle} = t_D + t_M + t_F$. In simulation, t_M and t_F are fixed to 0.02ns, while t_D is the only control variable.

The slow ramp stage (i) begins from a highly tilted double-well, with the particle trapped in the fluxoid state "-1" with certainty. The external flux, $\delta\phi_{\rm x}$ is then increased linearly with time from $\delta\phi_{\rm x} = -\delta\phi_{\rm xm} = -0.01$ to $\delta\phi_{\rm x} = 0$, at which point the potential is symmetric, with the slow ramp time $t_{\rm D}$. In terms of information theory, this corresponds to driving the system from $S_{\rm H} = 0$ to $S_{\rm H} = k_{\rm B}\ln 2$, where $S_{\rm H} = -k_{\rm B}\sum_{i=0,1} p(i)\ln p(i)$ is the Shannon entropy [168]. This process is equivalent to creating one bit of information. The system is driven quasi-statically from a zero bit configuration (particle trapped in a known state) to the one-bit configuration (two equally probable states). The thermodynamics of each cycle is characterized quantitatively by the work, W, performed by the engine and the heat absorbed, Q, from the thermal reservoir. In particular, when the slow ramp stage becomes quasi-static (the stage of creation of information), due to an increase in the inter-well transitions probability (thus decrease the time spent in the "-1" state), the engine absorbs net heat from the bath, while on average, the engine does a net negative work, $W_{\rm D}$.

In the measurement stage (ii), the system is idled at $\delta\phi_x = 0$ for a short duration $t_{\rm M}$, which is set by the time required to perform the measurement. For typical SQUIDs, $t_{\rm M}$ can be $1\,\mu$s or less. The flux particle position is then measured, e.g., by a magnetometer, to determine its state. The sole purpose is to determine if the system is in the logic state "-1" or "1". The net heat absorbed or released is always zero during the measurement stage because energies of the two states are equal, and so is the work done by the engine, $W_{\rm M} = 0$.

In the post-measurement fast ramp stage (iii), if the system is in the "-1" ("1") state the flux bias, $\delta\phi_x$ is then decreased (increased) rapidly to $-\delta\phi_{xm}$ ($\delta\phi_{xm}$). Due to the inversion symmetry of the potential energy, either path completes a thermodynamic cycle. The duration of the fast ramp stage must satisfy $\Gamma_0 t_{\rm F} << 1$ so that the system remains in the same flux state during stage (iii). As a result there is not enough time for inter-well transitions to occur so that the engine always does a positive work of $W_{\rm F} = U(\delta\phi_x = 0) - U(\delta\phi_x = \pm\delta\phi_{xm})$ in stage (iii). In the numerical simulation, the flux logic device is not required to wait for a long time $t_{\rm M}$ to determine its logic state, and the

fast ramp time is set to 0.02 ns. For a complete cycle, one has $W = Q$ according to the first law of thermodynamics.

4.4.2 Results and discussion

For each value of the damping parameter G, the simulation is performed by varying t_{cycle}. FIG. 4.10(a) shows the three individual trajectories for the under-damped case ($G = 0.1$) with the cycle time, t_{cycle}, 25 ns (red), 50 ns (cyan) and 300 ns (blue) respectively. The value of $\langle W \rangle / k_{\text{B}} T \ln 2$ for the trajectories shown are 0.68, 0.95 and 0.99 respectively. FIG. 4.10(b) shows the distribution for the above mentioned t_{cycle} obtained by repeating each protocol cycle $50,000$ times. The result shows that when $t_{\text{cycle}} \geq 300$ ns approaches the quasi-static limit, the distribution is a Gaussian centered at $k_{\text{B}} T \ln 2$.

FIG. 4.11 shows the average heat absorbed per cycle vs. the slow-ramp time t_{D} for four different values of the damping parameter G, where each data point is obtained by averaging over 5×10^4 simulated cycles. The standard error bar on each point is negligible. When t_{D} approaches the quasi-static limit, characterized by $\Gamma_0 t_{\text{D}} >> 1$, the average amount of heat absorbed per cycle, $\langle Q \rangle$, approaches the Landauer's limit $k_{\text{B}} T \ln 2$. According to information theory, this corresponds to driving the system from $S_{\text{H}} = 0$ to $S_{\text{H}} = k_{\text{B}} \ln 2$ as the Shannon entropy suggest $S = -k_{\text{B}} \sum_{i=0,1} p(i) \ln p(i)$ [168]. This process is equivalent to the creation of one bit of information, in which the system is driven quasi-statically from a zero bit configuration (particle trapped in a known state) to the one-bit configuration (two equally probable states). The plot shows that stronger damping requires longer t_{D} to reach the QS limit. For $G = 10$, it takes $t_{\text{D}} = 6000$ ns to reach $\langle Q \rangle = 0.95\, k_{\text{B}} T \ln 2$ while for $G = 0.1$, it only requires $t_{\text{D}} = 350$ ns. Furthermore, as t_{D} is decreased from Γ_0^{-1}, the average amount of heat absorbed from the heat bath per cycle decreases because less inter-well transitions occur. We observe a monotonic decrease in $\langle Q \rangle$ which ultimately reaches zero for respective cutoff drive time t_{D} depending on the value of G. It is convenient to define two time limits t_{C} and t_{QS} as

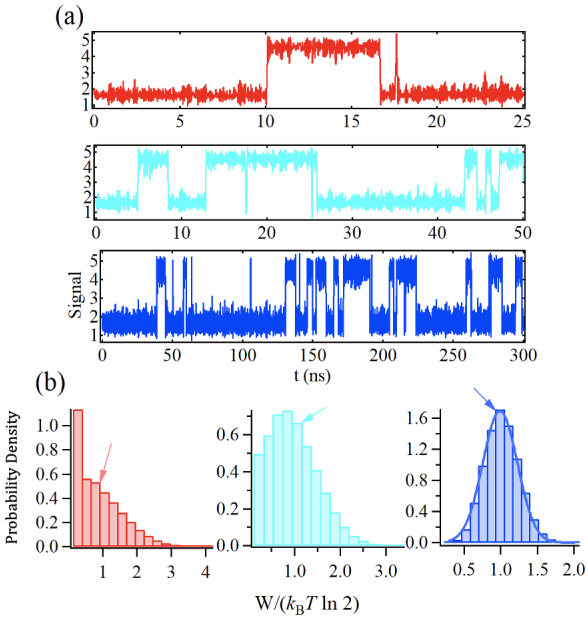

Figure 4.10. (a) Typical trajectories of the particle with cycle time 25 ns (red), 50 ns(cyan) and 300 ns (blue) respectively following the protocol is G-independent ($G = 0.1$). The value of $W/k_{\rm B}T\ln 2$ for the three trajectories shown are 0.68, 0.95 and 0.99 respectively. (b) The corresponding probability distribution of the work done is obtained by repeating the cycle for 50,000 times. The arrows indicate the work done by the engine associated with the three individual trajectories shown in (a).

the time when $\langle Q \rangle$ is 5% and 95% of the $k_{\rm B}T\ln 2$ respectively. The lower threshold $t_{\rm C}$ determines how fast the engine can be run in the drive stage. In addition, one must set $t_{\rm F} < t_{\rm C}$ to avoid inter-well transitions during the fast ramp stage. We find that for $G = 10$ (over-damped) and $G = 0.1$ (under-damped) case $t_{\rm C}$ is 10 and 1 ns, respectively.

Since we are also interested in studying the effect of damping on the thermodynamic quantities and Γ_0 is damping dependent, it is instructive to express $t_{\rm D}$ in units of Γ_0^{-1}. FIG. 4.12(a) shows $\langle W \rangle$ for different values of G vs. $\Gamma_0 t_{\rm D}$. Each data points are the average of 50,000 cycles shown with standard error, $\sigma_\mu \sim 10^{-3}$. Quantitatively, the process becomes quasi-static and the $\langle W \rangle \geq 0.95 k_{\rm B}T\ln 2$, when $t_{\rm QS} \equiv \Gamma_0 t_{\rm cycle} \geq 40$ irrespective of the damping strength. Also, the threshold time t_C is found to be 0.1 for all of the damping strengths.

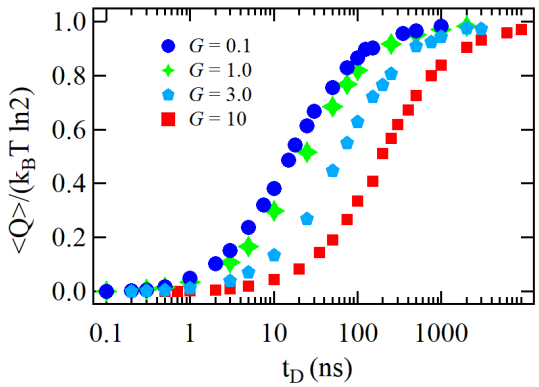

Figure 4.11. (a) $\langle Q \rangle$ by the logic device as a function of the cycle duration t_{cycle} for G= 0.1, 1.0, 3.0 and 10, corresponding to the under-damped, moderately damped and over-damped cases respectively. Each data point is averaged over $N = 50,000$ engine cycles. $\langle Q \rangle$ approaches the Landauer's limit, $k_{\text{B}}T\ln 2$, when the cycle time becoming quasi-static. It is clear that, for the over-damped case, the engine requires longer t_{cycle} to reach the quasi-static limit than the moderately and under-damped cases do.

We calculated the normalized power output, $P = (\langle W \rangle / k_{\text{B}}T)/\ \Gamma_0 t_{\text{D}}$, as shown in FIG. 4.12(b). The power increases as $\Gamma_0 t_{\text{D}}$ increase and eventually reaches a maximum value P_{max}, then starts to decrease with further increase of t_{D}. For $G = 0.1$, the optimal drive time to generate maximum power, P_{max} = 0.43, is at $t_{\text{max}} = \Gamma_0 t_{\text{D}}$= 0.18.

FIG. 4.13 shows the effect of temperature on $\langle W \rangle$ for a particular G = 0.1. The thermal activation rate, Γ_0 for T = 5 K is $1.68 \times 10^8/\text{s}$ which is twice as fast as at T = 4.2 K. However, when plotted against the normalized drive time they overlap each other within statistical uncertainties. This confirms to have no effect of T on $\langle W \rangle$.

In conclusion, we proposed a high-efficiency Szilard engine based on the flux logic device and investigated its properties numerically. It is found that the engine extracts $k_{\text{B}}T\ln 2$ heat, on average, per cycle in the quasi-static regime from the thermal reservoir when one-bit information is created, as predicted by Landauer's principle. Furthermore, our study reveals an important result that the output power of the engine is maximum when operated with an optimized speed $(\Gamma_0 t_{\text{D}})^{-1} \cong 5.5$,

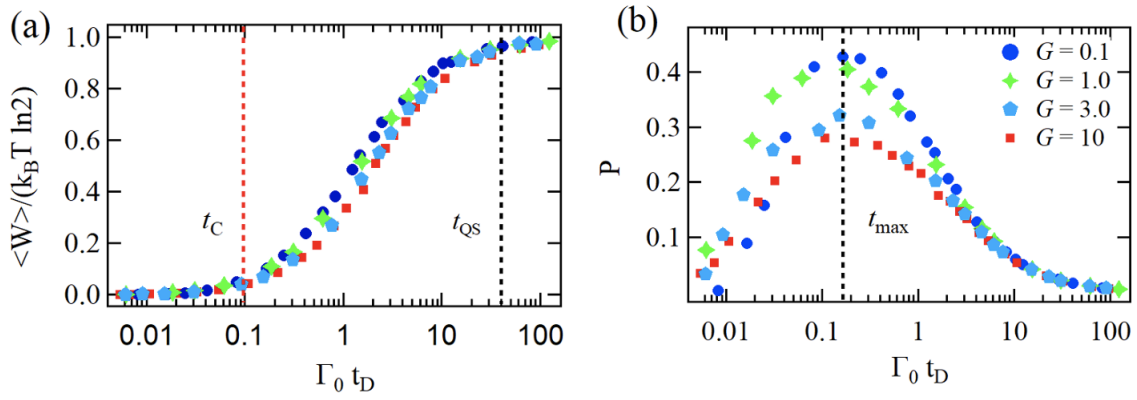

Figure 4.12. (a) Ensemble average of the work done by the logic device as a function of the normalized slow ramp time $\Gamma_0 t_D$ for under-damped (red), moderately damped (green) and over-damped (blue) cases defined by normalized damping parameter G. Each data point is the average of 50,000 engine cycles shown with standard error. t_C and t_{QS} are the two time limits such that $\langle W \rangle$ is 5 and 95% of the $k_B T \ln 2$ respectively. $\langle W \rangle / k_B T \ln 2$ approaches the Landauer's limit when the normalized slow ramp time becomes quasi-static. (b) The power output, P by the logic device as a function of the normalized slow ramp time $\Gamma_0 t_D$. The vertical dashed black line shows the location of the maximum power, $P_{max} = 0.43$ at an optimal $\Gamma_0 t_D = 0.18$ or the slow ramp time $t_D = 2.2\,\text{ns}$.

which is more than 200 times faster than the upper speed limit $(\Gamma_0 t_D)^{-1} \cong 0.025$ of the quasi-static regime. These findings provide valuable insights to the optimization of Szilard engines with information as fuel.

So far, in our discussion we have restricted our simulation using one-JJ rf SQUID. In reality, either one-JJ or two-JJ rf SQUID can be used. The future work can be extended to make the protocol more efficient, in which tilt and the barrier height are simultaneously varied. The ability to control the barrier height independently allows the Szilard engine to shorten the minimum drive time required to satisfy to reach the quasi-static condition [150]. Also, due to miniaturization of the device, it has become essential to extend stochastic thermodynamics in the quantum realm. It is possible to do the experiment in the quantum regime in which interwell transitions are caused

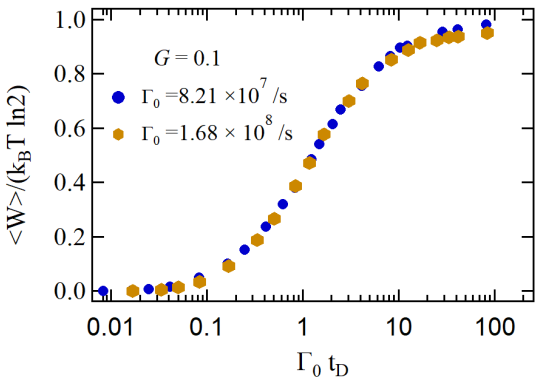

Figure 4.13. The average work done per cycle by the logic device for G = 0.1 at T =4.2 (blue) and 5 K (brown). The thermal activation rate, $\Gamma_0 = 1.68 \times 10^8/\text{s}$ and $8.21 \times 10^7/\text{s}$ for $T = 5\text{K}$ and 4.2 K respectively. The two curves overlap within statistical uncertainties showing no effect of T on $\langle W \rangle$ of the Szilard engine. Each data point is obtained by averaging $50,000$ thermodynamic cycles shown with 1σ error bar (however, they are difficult to see).

by quantum fluctuation and or/ quantum coherence. The open question is, can a quantum engine do more work than the limit set by the second law of thermodynamics?

Chapter 5

Summary

In summary, we studied the phase dynamics of moderately damped Josephson junctions. There are three states of the phase particle in tilted washboard potential, i.e., trapped, PD, and running state. Thus, there are two sequences of transition from the trapped state to the running state: (1) Direct; (2) via PD as the intermediate state. The particle can escape from the trapped state by either TA or MQT, depends on if T is above or below the crossover temperature T_{cr}. The subsequent motion can either be a direct switching to the running state or going through the intermediate PD state. In previous studies, the effect of damping, temperature, and the junction parameters E_J and E_c on PD is studied. While the role of potential tilt (i) has been mostly overlooked.

First, we observed MQT by measuring their switching current distributions (SCDs) between 50 mK and 3.0 K. The data show that T_{cr} of the junctions is $\sim$ 0.5-0.8 K reflecting the high characteristic plasma frequency ($\omega_{p0}/2\pi \sim$ THz), making them promising for microwave and terahertz applications. The results also show that the planar FHIB Y-Ba-Cu-O junction is promising for scalable quantum circuit.

Second, we observed the distinctive signature of phase diffusion, as the appearance of an anti-correlation between temperature and the width of the SCDs at $T > T_{cr}$. After escaping from the

initial potential well repeated escapes and retrapping lead to phase diffusion. PD is facilitated small bias current and high temperatures. Thus it is necessary to provide a larger tilt to the potential to allow the junction to switch to the running state. Therefore, above T_{cr} the experimental value of $\langle I_{\rm s}\rangle$ are larger than the mean escape current, $\langle I_{\rm esc}\rangle$ expected from TA.

Furthermore, the effect of potential tilt in determining the phase dynamics of the Josephson junctions are studied by scanning the parameter space $(i, k_{\rm B}T/E_J)$. We compare the mean escape current, $\langle I_{\rm esc}\rangle$ predicted by TA and MQT for junctions having different E_J/E_C but same Q_0. Junctions with larger E_J, but otherwise having the same Q_0, require greater tilt to transit to MQT from TA or the PD regime. Thus, in experiments, one observes higher switching currents in the presence of PD.

Finally, we showed that the SQUID-based flux logic device can be modeled as a one-bit memory, making an ideal prototype for constructing Szilard engines with unprecedented speed and performance. First, the proposed engine can extract 95% of $k_{\rm B}T\ln 2$, on average, of work $\langle W\rangle$ per cycle from the thermal reservoir in the quasi-static (QS) limit, $t_{\rm QS} = 350\,{\rm ns}$, where $t_{\rm QS}$ is the cycle time. In the QS limit, the engine has sufficient time to thermalize with the thermal bath to absorb more heat through multiple inter-well transitions. However, the engine operating in the QS limit is slow because although it maximizes the work done per cycle, it sacrifices speed and the combined effect results in a lower power P. Furthermore, we found that the lower bound of the drive limit $t_C = 1\,{\rm ns}$, at which $\langle W\rangle$ is 5% of $k_{\rm B}T\ln 2$, which again leads to poor performance in terms of power. In between these two extreme limits, we identify an optimal cycle time, $t_{\rm cycle} = 1.8\,{\rm ns}$, which produces maximum power desirable for many applications. Our result demonstrates that FLD-based Szilard engines' performance can exceed other nano-device implementations by orders of magnitude.

To sum up, this dissertation covers the study of the phase dynamics of moderately damped planar FHIB Y-Ba-Cu-O Josephson junctions. Different regimes are identified from the statistical property of the SCDs through well-defined criteria. The observation of MQT in such junctions

opens a way to explore and test other macroscopic quantum effects. Also, SQUID based flux logic device as a Szilard engine is not yet realized in the quantum realm. Thus, such devices may provide an excellent platform to understand quantum thermodynamics.

Bibliography

[1] A. Barone and G. Paterno, *Physics and applications of the Josephson effect* (Wiley, 1982).

[2] T. Friedmann, M. Rabin, J. Giapintzakis, J. Rice, and D. Ginsberg, Phys. Rev. B **42**, 6217 (1990).

[3] E. Maxwell, Phys. Rev. **78**, 477 (1950).

[4] J. Clarke, in *SQUID sensors: fundamentals, fabrication and applications* (Springer, 1996) pp. 1–62.

[5] J. Clarke, in *The new superconducting electronics* (Springer, 1993) pp. 123–180.

[6] K. K. Likharev and V. K. Semenov, IEEE Trans. Appl. Supercond. **1**, 3 (1991).

[7] W. Chen, A. Rylyakov, V. Patel, J. Lukens, and K. Likharev, IEEE Trans. Appl. Supercond. **9**, 3212 (1999).

[8] J. Sarrao, W. Kwok, I. Bozovic, *et al.*, in *Report of the Basic Energy Sciences Workshop on Superconductivity* (sn, 2006) pp. 8–11.

[9] V. L. Ginzburg and L. D. Landau, in *On Superconductivity and Superfluidity* (Springer, 2009) pp. 113–137.

[10] M. Tinkham, *Introduction to superconductivity* (Courier Corporation, 2004).

[11] C. Kittel, *Introduction to solid state physics* (John Wiley and Sons, 2004).

[12] L. P. Gor'kov, Sov. Phys. JETP **9**, 1364 (1959).

[13] H. Fröhlich, Nature **228**, 1145 (1970).

[14] P. W. Anderson, in *J .Phys. Conf. Ser.*, Vol. 449 (2013) p. 012001.

[15] K. J. Leary, H.-C. Zur Loye, S. W. Keller, T. A. Faltens, W. K. Ham, J. N. Michaels, and A. M. Stacy, Phys. Rev. Lett. **59**, 1236 (1987).

[16] J. Bardeen, L. N. Cooper, and J. R. Schrieffer, Phys. Rev. **108**, 1175 (1957).

[17] D. Averin and K. Likharev, J. Low Temp. Phys. **62**, 345 (1986).

[18] G. Binnig and H. Rohrer, Rev. Mod. Phys. **59**, 615 (1987).

[19] P. Benioff, J. Stat. Phys. **22**, 563 (1980).

[20] E. L. Wolf, *Principles of electron tunneling spectroscopy*, Vol. 152 (Oxford University Press, 2012).

[21] A. Feshchenko, J. Koski, and J. P. Pekola, Phys. Rev. B **90**, 201407 (2014).

[22] K. Likharev, Rev. Mod. Phys. **51**, 101 (1979).

[23] T. Klapwijk, J. Supercond. **17**, 593 (2004).

[24] J. P. Pekola and I. M. Khaymovich, Annu. Rev. Condens. Matter Phys. **10**, 193 (2019).

[25] F. Giazotto, T. T. Heikkilä, A. Luukanen, A. M. Savin, and J. P. Pekola, Rev. Mod. Phys. **78**, 217 (2006).

[26] B. D. Josephson, Phys. Lett. **1**, 251 (1962).

[27] I. Giaever, Phys. Rev. Lett. **5**, 147 (1960).

[28] P. W. Anderson and J. M. Rowell, Phys. Rev. Lett. **10**, 230 (1963).

[29] V. Ambegaokar and A. Baratoff, Phys. Rev. Lett. **10**, 486 (1963).

[30] R. P. Feynman, R. B. Leighton, and M. Sands, Am. J. Phys. **33**, 750 (1965).

[31] B. Taylor, W. Parker, D. Langenberg, and A. Denenstein, Metrologia **3**, 89 (1967).

[32] S. Shapiro, Phys.Rev. Lett. **11**, 80 (1963).

[33] W. C. Stewart, Appl. Phys. Lett. **12**, 277 (1968).

[34] D. E. McCumber, J. Appl. Phys. **39**, 3113 (1968).

[35] J. M. Martinis and R. L. Kautz, Phys. Rev. Lett. **63**, 1507 (1989).

[36] A. O. Caldeira and A. J. Leggett, Ann. Phys. **149**, 374 (1983).

[37] D. Massarotti, A. Pal, G. Rotoli, L. Longobardi, M. G. Blamire, and F. Tafuri, Nat. Commun. **6**, 7376 (2015).

[38] G.-H. Lee, D. Jeong, J.-H. Choi, Y.-J. Doh, and H.-J. Lee, Phys. Rev. Lett. **107**, 146605 (2011).

[39] H. Grabert and U. Weiss, Phys. Rev. Lett. **53**, 1787 (1984).

[40] J. M. Martinis, M. H. Devoret, and J. Clarke, Nat. Phys. **16**, 234 (2020).

[41] H. A. Kramers, Physica **7**, 284 (1940).

[42] M. Büttiker, E. Harris, and R. Landauer, Phys. Rev. B **28**, 1268 (1983).

[43] A. O. Caldeira and A. J. Leggett, Phys. Rev. Lett. **46**, 211 (1981).

[44] J. M. Martinis, M. H. Devoret, and J. Clarke, Phys. Rev. Lett. **55**, 1543 (1985).

[45] A. N. Cleland, J. M. Martinis, and J. Clarke, Phys. Rev. B **37**, 5950 (1988).

[46] H. Grabert and U. Weiss, Phys. Rev. Lett. **53**, 1787 (1984).

[47] R. L. Kautz and J. M. Martinis, Phys. Rev. B **42**, 9903 (1990).

[48] H. F. Yu, X. B. Zhu, H. Deng, G. M. Xue, Y. Tian, Y. F. Ren, G. H. Chen, D. N. Zheng, X. N. Jing, L. Lu, S. P. Zhao, and S. Han, J. Phys. Conf. Ser. **400**, 042079 (2012).

[49] J. Kivioja, T. Nieminen, J. Claudon, O. Buisson, F. Hekking, and J. P. Pekola, New J. Phys. **7**, 179 (2005).

[50] M. Constantin and C. C. Yu, Phys. Rev. Lett. **99**, 207001 (2007).

[51] T. Fulton and L. Dunkleberger, Phys. Rev. B **9**, 4760 (1974).

[52] S.-X. Li, W. Qiu, S. Han, Y. F. Wei, X. B. Zhu, C. Z. Gu, S. P. Zhao, and H. B. Wang, Phys. Rev. Lett. **99**, 037002 (2007).

[53] H. Yu, X. Zhu, Z. Peng, Y. Tian, D. Cui, G. Chen, D. Zheng, X. Jing, L. Lu, S. Zhao, *et al.*, Phys. Rev. Lett. **107**, 067004 (2011).

[54] T. Orlando, J. Mooij, L. Tian, C. H. Van Der Wal, L. Levitov, S. Lloyd, and J. Mazo, Phys. Rev. B **60**, 15398 (1999).

[55] R. Harris, J. Johansson, A. Berkley, M. Johnson, T. Lanting, S. Han, P. Bunyk, E. Ladizinsky, T. Oh, I. Perminov, *et al.*, Phys. Rev. B **81**, 134510 (2010).

[56] J. R. Friedman, V. Patel, W. Chen, S. Tolpygo, and J. E. Lukens, Nat. Phys. **406**, 43 (2000).

[57] S. Han, J. Lapointe, and J. Lukens, Physical review letters **63**, 1712 (1989).

[58] G. Li, S. Dhamala, H. Li, J. Liu, and W. Chen, Chin. Phys. B **27**, 068501 (2018).

[59] S. A. Cybart, S. Wu, S. Anton, I. Siddiqi, J. Clarke, and R. Dynes, Appl. Phys. Lett. **93**, 182502 (2008).

[60] S. A. Cybart, S. M. Anton, S. M. Wu, J. Clarke, and R. C. Dynes, Nano Lett. **9**, 3581 (2009).

[61] E. Y. Cho, Y. W. Zhou, J. Y. Cho, and S. A. Cybart, Appl. Phys. Lett. **113**, 022604 (2018).

[62] H. Li, H. Cai, E. Y. Cho, S. J. McCoy, Y.-T. Wang, J. C. LeFebvre, Y. W. Zhou, and S. A. Cybart, Appl. Phys. Lett. **116**, 070601 (2020).

[63] B. Ward, J. A. Notte, and N. Economou, J. Vac. Sci. Technol. B **24**, 2871 (2006).

[64] W. Lang, M. Dineva, M. Marksteiner, T. Enzenhofer, K. Siraj, M. Peruzzi, J. Pedarnig, D. Bäuerle, R. Korntner, E. Cekan, *et al.*, Microelectron. Eng. **83**, 1495 (2006).

[65] E. Mitchell, K. Hannam, J. Lazar, K. Leslie, C. Lewis, A. Grancea, S. Keenan, S. Lam, and C. Foley, Supercond. Sci. Technol. **29**, 06LT01 (2016).

[66] A. J. Leggett, Progress of Theoretical Physics Supplement **69**, 80 (1980).

[67] J. M. Martinis, M. H. Devoret, and J. Clarke, Phys. Rev. B **35**, 4682 (1987).

[68] M. H. Devoret, J. M. Martinis, and J. Clarke, Phys. Rev. Lett. **55**, 1908 (1985).

[69] R. F. Voss and R. A. Webb, Phys. Rev. Lett. **47**, 265 (1981).

[70] D. Schwartz, B. Sen, C. N. Archie, and J. Lukens, Phys. Rev. Lett. **55**, 1547 (1985).

[71] S. Washburn, R. A. Webb, R. Voss, and S. Faris, Phys. Rev. Lett. **54**, 2712 (1985).

[72] D. Vion, M. Götz, P. Joyez, D. Esteve, and M. Devoret, Phys. Rev. Lett. **77**, 3435 (1996).

[73] R. Rouse, S. Han, and J. Lukens, Phys. Rev. Lett. **75**, 1614 (1995).

[74] Y. Makhlin, G. Schön, and A. Shnirman, Rev. Mod. Phys. **73**, 357 (2001).

[75] C. Tsuei and J. Kirtley, Rev. Mod. Phys. **72**, 969 (2000).

[76] Y. Tanaka and S. Kashiwaya, Phys. Rev. Lett. **74**, 3451 (1995).

[77] L. Longobardi, D. Massarotti, D. Stornaiuolo, L. Galletti, G. Rotoli, F. Lombardi, and F. Tafuri, Phys. Rev. Lett. **109**, 050601 (2012).

[78] H. R. Yi, D. Winkler, and T. Claeson, Appl. Phys. Lett. **68**, 2562 (1996).

[79] T. Bauch, F. Lombardi, F. Tafuri, A. Barone, G. Rotoli, P. Delsing, and T. Claeson, Phys. Rev. Lett. **94**, 087003 (2005).

[80] D. Massarotti, L. Longobardi, L. Galletti, D. Stornaiuolo, G. Rotoli, and F. Tafuri, Low Temp. Phys. **39**, 294 (2013).

[81] K. Inomata, S. Sato, K. Nakajima, A. Tanaka, Y. Takano, H. Wang, M. Nagao, H. Hatano, and S. Kawabata, Phys. Rev. Lett. **95**, 107005 (2005).

[82] X. Jin, J. Lisenfeld, Y. Koval, A. Lukashenko, A. Ustinov, and P. Müller, Phys. Rev. lett. **96**, 177003 (2006).

[83] H. Kashiwaya, T. Matsumoto, H. Shibata, S. Kashiwaya, H. Eisaki, Y. Yoshida, S. Kawabata, and Y. Tanaka, J. Phys. Soc. Japan **77**, 104708 (2008).

[84] S. Sato, K. Inomata, M. Kinjo, N. Kitabatake, K. Nakajima, H. Wang, and T. Hatano, IEICE Trans. **90**, 599 (2007).

[85] M. H. Devoret and R. J. Schoelkopf, Science **339**, 1169 (2013).

[86] P. Krantz, M. Kjaergaard, F. Yan, T. P. Orlando, S. Gustavsson, and W. D. Oliver, App. Phys. Rev. **6**, 021318 (2019).

[87] P. Krantz, M. Kjaergaard, F. Yan, T. P. Orlando, S. Gustavsson, and W. D. Oliver, Appl. Phys. Rev. **6**, 021318 (2019).

[88] I. Joel, J. Wang, D. Rodan-Legrain, L. Bretheau, D. L. Campbell, B. Kannan, D. Kim, M. Kjaergaard, P. Krantz, G. O. Samach, *et al.*, Nat. Nanotechnol. **14**, 120 (2019).

[89] L. Casparis, M. R. Connolly, M. Kjaergaard, N. J. Pearson, A. Kringhøj, T. W. Larsen, F. Kuemmeth, T. Wang, C. Thomas, S. Gronin, *et al.*, Nat. Nanotechnol. **13**, 915 (2018).

[90] L. Grünhaupt, M. Spiecker, D. Gusenkova, N. Maleeva, S. T. Skacel, I. Takmakov, F. Valenti, P. Winkel, H. Rotzinger, W. Wernsdorfer, *et al.*, Nat. Mater **18**, 816 (2019).

[91] S. A. Cybart, E. Y. Cho, T. J. Wong, B. H. Wehlin, M. K. Ma, C. Huynh, and R. C. Dynes, Nat. Nanotechnol. **10**, 598 (2015).

[92] B. Müller, M. Karrer, F. Limberger, M. Becker, B. Schröppel, C. J. Burkhardt, R. Kleiner, E. Goldobin, and D. Koelle, Phys. Rev. Appl. **11**, 044082 (2019).

[93] J. C. LeFebvre, E. Cho, H. Li, K. Pratt, and S. A. Cybart, AIP Adv. **9**, 105215 (2019).

[94] J. G. Bednorz and K. A. Müller, Zeitschrift für Physik B Condensed Matter **64**, 189 (1986).

[95] D. Lundy, L. Swartzendruber, and L. Bennett, Journal of research of the national institute of standards and technology **94**, 147 (1989).

[96] C. Park and R. L. Snyder, J. Am. Ceram. Soc. **78**, 3171 (1995).

[97] T. Dinger, T. Worthington, W. Gallagher, and R. Sandstrom, Phys. Rev. Lett. **58**, 2687 (1987).

[98] T. K. Worthington, W. Gallagher, and T. Dinger, Phys. Rev. Lett. **59**, 1160 (1987).

[99] W. E. Booij, A. J. Pauza, E. J. Tarte, D. F. Moore, and M. G. Blamire, Phys. Rev. B **55**, 14600 (1997).

[100] D. Dimos, P. Chaudhari, J. Mannhart, and F. LeGoues, Phys. Rev. Lett. **61**, 219 (1988).

[101] K. Char, M. Colclough, S. Garrison, N. Newman, and G. Zaharchuk, Appl. Phys. Lett. **59**, 733 (1991).

[102] C. Foley, E. Mitchell, S. Lam, B. Sankrithyan, Y. Wilson, D. Tilbrook, and S. Morris, IEEE Trans. Appl. Supercond. **9**, 4281 (1999).

[103] F. Tafuri, *Fundamentals and Frontiers of the Josephson Effect*, Vol. 286 (Springer Nature, 2019).

[104] S. Adachi, A. Tsukamoto, Y. Oshikubo, and K. Tanabe, IEEE Trans. Appl. Supercond. **26**, 1 (2016).

[105] H. Hilgenkamp and J. Mannhart, Rev. Mod. Phys. **74**, 485 (2002).

[106] J. Zaanen, S. Chakravarty, T. Senthil, P. Anderson, P. Lee, J. Schmalian, M. Imada, D. Pines, M. Randeria, C. Varma, *et al.*, Nat. Phys. **2**, 138 (2006).

[107] R. C. Richardson, *Experimental techniques in condensed matter physics at low temperatures* (CRC Press, 2018).

[108] J. C. Wheatley, O. Vilches, and W. Abel, Physics Physique Fizika **4**, 1 (1968).

[109] O. Lounasmaa, J. Phys. E Sci. Instrum. **12**, 668 (1979).

[110] H. London, G. Clarke, and E. Mendoza, Phys. Rev. **128**, 1992 (1962).

[111] D. G. Batey and D. G. Teleberg, (2015).

[112] B. Mao, *Coherent Manipulation of Multi-Partite Quantum States in a Qubit-TLS System via Landau-Zener Transition*, Ph.D. thesis, University of Kansas (2010).

[113] S.-X. Li, Y. Yu, Y. Zhang, W. Qiu, S. Han, and Z. Wang, Phys. Rev. Lett. **89**, 098301 (2002).

[114] J. Männik, S. Li, W. Qiu, W. Chen, V. Patel, S. Han, and J. Lukens, Phys. Rev. B **71**, 220509 (2005).

[115] J. Fenton and P. Warburton, Phys. Rev. B **78**, 054526 (2008).

[116] P. Hänggi and F. Marchesoni, Rev. Mod. Phys. **81**, 387 (2009).

[117] G. S. Kottas, L. I. Clarke, D. Horinek, and J. Michl, Chem. Rev. **105**, 1281 (2005).

[118] M. Iansiti, M. Tinkham, A. Johnson, W. F. Smith, and C. Lobb, Phys. Rev. B **39**, 6465 (1989).

[119] E. Pollak, J. Bader, B. Berne, and P. Talkner, Phys. Rev. Lett. **70**, 3299 (1993).

[120] M. Bier, Contemp. Phys. **38**, 371 (1997).

[121] M. Sivan and O. Farago, Phys. Rev. E **98**, 052117 (2018).

[122] E. Ben-Jacob, D. Bergman, B. Matkowsky, and Z. Schuss, Phys. Rev. A **26**, 2805 (1982).

[123] A. Franz, Y. Koval, D. Vasyukov, P. Müller, H. Schneidewind, D. Ryndyk, J. Keller, and C. Helm, Phys. Rev. B **69**, 014506 (2004).

[124] A. A. Golubov, M. Y. Kupriyanov, and E. Il'Ichev, Rev. Mod. Phys. **76**, 411 (2004).

[125] J. M. Martinis and R. L. Kautz, Phys. Rev. Lett. **63**, 1507 (1989).

[126] D. Stornaiuolo, G. Rotoli, D. Massarotti, F. Carillo, L. Longobardi, F. Beltram, and F. Tafuri, Phys. Rev. B **87**, 134517 (2013).

[127] G. Rotoli, T. Bauch, T. Lindstrom, D. Stornaiuolo, F. Tafuri, and F. Lombardi, Phys. Rev. B **75**, 144501 (2007).

[128] P. Silvestrini, S. Pagano, R. Cristiano, O. Liengme, and K. Gray, Phys. Rev. Lett. **60**, 844 (1988).

[129] V. Krasnov, T. Bauch, S. Intiso, E. Hürfeld, T. Akazaki, H. Takayanagi, and P. Delsing, Phys. Rev. Lett. **95**, 157002 (2005).

[130] J. B. Johnson, Phys. Rev. **32**, 97 (1928).

[131] J. Männik, S. Li, W. Qiu, W. Chen, V. Patel, S. Han, and J. E. Lukens, Phys. Rev. B **71**, 220509 (2005).

[132] Y. Yoon, S. Gasparinetti, M. Möttönen, and J. Pekola, J. Low Temp. Phys. **163**, 164 (2011).

[133] L. Longobardi, D. Massarotti, G. Rotoli, D. Stornaiuolo, G. Papari, A. Kawakami, G. P. Pepe, A. Barone, and F. Tafuri, Phys. Rev. B **84**, 184504 (2011).

[134] L. Longobardi, D. Stornaiuolo, D. Massarotti, G. Rotoli, L. Galletti, and F. Tafuri, IEEE Trans. Appl. Supercond. **25**, 1 (2015).

[135] R. Kubo, Rep. Prog. Phys. **29**, 255 (1966).

[136] S. Han, J. Lapointe, and J. Lukens, Phys. Rev. B **46**, 6338 (1992).

[137] L. Szilard, J. Phys. **53**, 840 (1929).

[138] C. H. Bennett, Int. J. Theor. Phys. **21**, 905 (1982).

[139] S. Lloyd, Nature **406**, 1047 (2000).

[140] K. Maruyama, F. Nori, and V. Vedral, Rev. Mod. Phys. **81**, 1 (2009).

[141] E. Lutz and S. Ciliberto, Phys. Today **68**, 30 (2015).

[142] R. Landauer, IBM J. Res. Dev. **5**, 183 (1961).

[143] I. A. Martínez, É. Roldán, L. Dinis, D. Petrov, J. M. Parrondo, and R. A. Rica, Nat. Phys. **12**, 67 (2016).

[144] A. Bérut, A. Arakelyan, A. Petrosyan, S. Ciliberto, R. Dillenschneider, and E. Lutz, Nature **483** (2012).

[145] J. V. Koski, V. F. Maisi, J. P. Pekola, and D. V. Averin, Proc. Natl. Acad. Sci. **111**, 13786 (2014).

[146] S. Toyabe, T. Sagawa, M. Ueda, E. Muneyuki, and M. Sano, Nat. Phys. **6**, 988 (2010).

[147] T. Sagawa and M. Ueda, Phys. Rev. Lett. **102**, 250602 (2009).

[148] B. Piechocinska, Phys. Rev. A **61**, 062314 (2000).

[149] M. G. Raizen, Science **324**, 1403 (2009).

[150] O.-P. Saira, M. H. Matheny, R. Katti, W. Fon, G. Wimsatt, J. P. Crutchfield, S. Han, and M. L. Roukes, Phys. Rev. Research **2**, 013249 (2020).

[151] U. Seifert, Rep. Prog. Phys. **75**, 126001 (2012).

[152] M. Campisi, P. Hänggi, and P. Talkner, Rev. Mod. Phys. **83**, 771 (2011).

[153] V. Serreli, C.-F. Lee, E. R. Kay, and D. A. Leigh, Nature **445**, 523 (2007).

[154] D. Carberry, J. C. Reid, G. Wang, E. M. Sevick, D. J. Searles, and D. J. Evans, Phys. Rev. Lett. **92**, 140601 (2004).

[155] O.-P. Saira, Y. Yoon, T. Tanttu, M. Möttönen, D. Averin, and J. P. Pekola, Phys. Rev. Lett. **109**, 180601 (2012).

[156] J. V. Koski and J. P. Pekola, C. R. Phys. **17**, 1130 (2016).

[157] J. V. Koski, A. Kutvonen, I. M. Khaymovich, T. Ala-Nissila, and J. P. Pekola, Phys. Rev. Lett. **115**, 260602 (2015).

[158] A. Clark, A. Williams, S. Ruggiero, M. L. van den Berg, and J. N. Ullom, Appl. Phys. Lett. **84**, 625 (2004).

[159] J. P. Pekola, F. Giazotto, and O.-P. Saira, Phys. Rev. Lett. **98**, 037201 (2007).

[160] V. Blickle and C. Bechinger, Nat. Phys. **8**, 143 (2012).

[161] S. Ciliberto, Phys. Rev. X **7**, 021051 (2017).

[162] H.-T. Quan, Y.-x. Liu, C.-P. Sun, and F. Nori, Phys. Rev. E **76**, 031105 (2007).

[163] T. D. Kieu, Phys. Rev. Lett. **93**, 140403 (2004).

[164] N. Cottet, S. Jezouin, L. Bretheau, P. Campagne-Ibarcq, Q. Ficheux, J. Anders, A. Auffèves, R. Azouit, P. Rouchon, and B. Huard, Proc. Natl. Acad. Sci. **114**, 7561 (2017).

[165] O. Maillet, P. A. Erdman, V. Cavina, B. Bhandari, E. T. Mannila, J. T. Peltonen, A. Mari, F. Taddei, C. Jarzynski, V. Giovannetti, *et al.*, Phys. Rev. Lett. **122**, 150604 (2019).

[166] J. Clarke and A. I. Braginski, *The SQUID handbook: Applications of SQUIDs and SQUID systems* (John Wiley & Sons, 2006).

[167] J. P. Pekola, Nat. Phys. **11**, 118 (2015).

[168] J. Lin, IEEE Trans. on Inf. Theory **37**, 145 (1991).

Appendix A

Code for simulating Szilard engine

Code to simulate a flux logic device as a fast Szilard engine for optimal power

April 7, 2021

[1]:
```
""" Coded by Suman Dhamala @03/10/2020
A flux logic device is implemented as a fast Szilard engine for optimal power.
The Langevin equation of motion for a 1D flux logic device is solved using the
finite difference technique. The Nyquist noise current follows the fluctuation
dissipation theorem. Moreover, the random process is modeled to follow Gaussian
noise distribution. """

# import the useful libraries for the simulation
# import pandas as pd
import numpy as np
import matplotlib.pyplot as plt
from scipy.optimize import fsolve
from scipy.optimize import curve_fit
#from lmfit import Model
#import seaborn as sea
import operator
import math
pi = math.pi
```

[2]:
```
# Four independent parameter I_c, C, R and L of the flux logic device
L = 100*1.0e-12    # Inductance in H
I_c0 = 4.9e-06     # Critical current in A
C = 1200e-15       # Capacitance in F
G = 0.1            # Normalized damping parameter

# Deduced parameters beta0/E_J/U0/Omega_p0/G
flux_quantum =  2.068*1.0e-15;
k_B = 1.3807e-23 # Boltzmann constant value
beta0 = 2*pi*L*I_c0/flux_quantum  # shape determining parameter
U_0 = (flux_quantum)**2/(4*pi**2* L)   # Energy scale
E_J = ( U_0*beta0 )  # Josephson energy
Omega_p0 = np.sqrt(2*pi*I_c0/(flux_quantum*C)) # Angular frequency at zero bias
plasma_f0 = Omega_p0/(2*pi) # Plasma frequency
R = 1/(Omega_p0*G*C) # Resistance in the unit of ohm
```

[3]:
```
# For this parameters find DU0 (barrier height for phix=0.5 and beta0)
# For the given parameter find epsilon (tilt) for phix=-0.49 and beta0
# Find left, saddle and right position of the fictitious flux particle
# in the potential well for phix=-0.49 and beta0

phix_symmetric = 0.5*2*pi
phix_start = 0.49*2*pi
pot_energy_scale = U_0/k_B
T = 4.2

## derivative of  1 dim. potential
def pot_derv(self):
    return (self - phix_start) + beta0* np.sin(self)

## Make a starting guess
init_position = np.array([1.6,3,4.65 ])  # initial guess for phix=0.49/beta0
position = fsolve(pot_derv, init_position)

## finding potential energy value
def pot_energy(self,phix):
    return pot_energy_scale*( 0.5*( self- phix )**2  - beta0* np.cos(self) )

Uvalue_phix_start = pot_energy(position, phix_start)
Uvalue_phix_symmetric = pot_energy(position, phix_symmetric)

##
phi_L = position[0] # position in the left well
phi_R = position[2]
phi_saddle = position[1]
DU0 =  Uvalue_phix_symmetric[1]- Uvalue_phix_symmetric[0]  # barrier height for␣
↪symmetric potential
Exponent_factor = DU0/T #Exponential factor in the Arrehinious equation
Epsilon_start = (Uvalue_phix_start[0]-Uvalue_phix_start[2])/T
#print(position)
#print(Epsilon_start,DU0)
```

[4]:
```
# Variables
N_trials = 1 # Number of for loop iterations
dtau = (2*pi/250) # Normalized time step determined from convergence test

#Changing time for each part of the protocol
slow_ramp_time = 200*1.0e-9; # Variable slow ramp time in s
dwell_time = 0.02*1.0e-9; # fixed measurment time in s
fast_ramp_time = 0.02*1.0e-9; # fixed fast ramp time in s

#
a_t = np.sqrt(1+G**2/4)-G/2 #Damping constant in the Arrehenious equation
```

```
Gamma_0 = a_t*plasma_f0* np.exp(-Exponent_factor) #Rate from Arrehenius law
Thermalization_condition = Gamma_0*dwell_time*1.0e-9   #condition is
 ↪Gamma_0*t_dwell>>1

#Convert real time to normalized time for simulation
norm_slow_ramp_time = slow_ramp_time*Omega_p0
norm_dwell_time = dwell_time*Omega_p0
norm_fast_ramp_time = fast_ramp_time*Omega_p0

# Convert time series to points
N_slowramp = round(norm_slow_ramp_time/dtau)  # no. of data points for slow ramp
N_dwell = round(norm_dwell_time/dtau)    #No. of points in flat part
N_fastramp = round(norm_fast_ramp_time/dtau) #No. of points in fast ramp
feedback_point = ( N_slowramp + N_dwell)  # feedback point
Tau = (N_slowramp + N_dwell + N_fastramp )*dtau  # normalized total time
Tau_array = np.arange(0,Tau,dtau)
realtime_array = (Tau_array)/(Omega_p0)/1.0e-9 ; # converted to nanosecond

# Creating array of External flux and Energy bias according to conditional
 ↪feedback
Phix1_end = phix_symmetric + (phix_symmetric-phix_start)
phix_slow = np.linspace(phix_start, phix_symmetric, N_slowramp)
phix_dwell = np.ones(N_dwell,)*phix_symmetric
phix1_fast = np.linspace(phix_symmetric+(phix_slow[2]-phix_slow[1]), Phix1_end,
 ↪N_fastramp )
phix0_fast = np.linspace(phix_symmetric-(phix_slow[2]-phix_slow[1]),
 ↪phix_start, N_fastramp )

##
phix0_array = np.concatenate((phix_slow, phix_dwell, phix0_fast))
phix1_array = np.concatenate((phix_slow, phix_dwell, phix1_fast))

## creating Epsilon
Epsilon_slow = np.linspace(Epsilon_start, 0, N_slowramp)
Epsilon_dwell = np.zeros(N_dwell,)
Epsilon0_fast = np.linspace(0-(Epsilon_slow[2]-Epsilon_slow[1]), Epsilon_start,
 ↪N_fastramp )
Epsilon1_fast = np.linspace(0+(Epsilon_slow[2]-Epsilon_slow[1]),
 ↪-Epsilon_start, N_fastramp )

### Addaing each part to make an Array of phi_x and energy bias
Epsilon0_array = np.concatenate( (Epsilon_slow, Epsilon_dwell, Epsilon0_fast) )
Epsilon1_array = np.concatenate( (Epsilon_slow, Epsilon_dwell, Epsilon1_fast) )

##
from matplotlib import rc
```

```
rc('font', **{'family':'serif','serif':['Palatino']})
rc('text', usetex=True)
fig, ax = plt.subplots(nrows=1, ncols=2, sharey=False,figsize=(12,5))
# plots
ax[0].plot(realtime_array,phix0_array/(2*pi),color="blue", linewidth=1.0,␣
↪linestyle="-")
ax[0].plot(realtime_array,phix1_array/(2*pi),color="red", linewidth=1.0,␣
↪linestyle="-")
ax[1].plot(realtime_array,Epsilon0_array,color="blue", linewidth=1.0,␣
↪linestyle="-")
ax[1].plot(realtime_array,Epsilon1_array,color="red", linewidth=1.0,␣
↪linestyle="-")
# labels
ax[0].set_ylabel(r'$\phi_{x}$',fontsize=18)
ax[0].set_xlabel('time (ns)',fontsize=18)
ax[1].set_ylabel(r'$\epsilon/k_{B}T$',fontsize=18)
ax[1].set_xlabel('time (ns)',fontsize=18)
# adjust right subfigure axes location
ax[1].yaxis.tick_right()
ax[1].yaxis.set_label_position("right")
# figure settings
fig.suptitle('External flux bias and the energy bias', fontsize=18)
fig.tight_layout()
fig.subplots_adjust(top=0.9) # tight_layout ignores overall titles (current bug)
```

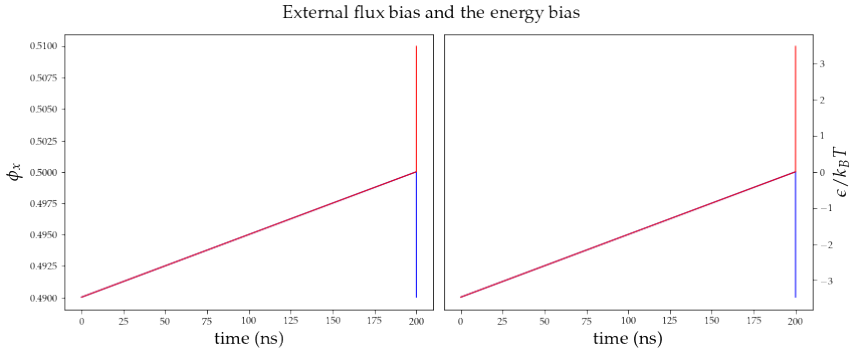

[5]:
```
# Langevin equation constant terms
inv_beta0 = 1/beta0 # inverse of beta0
dtau2 = dtau**2   # square of the normalized time
dtau3 = dtau**3   #cube of the normalized time
C1 = inv_beta0*dtau2   #constant term for phix_x term
C2 = 2-G*dtau-C1     #constant term for phi_n term
```

```
C3 = G*dtau-1      #constant term for phi_n-1 term
C4 = dtau2         #constant term for sin(phi_n)term
C5 = np.sqrt(2*G*k_B*T*dtau3/E_J)   #Noise amplitude

## Initialization of array
phi = np.zeros((len(phix1_array),))
Work_array = np.zeros((N_trials,))
Heat_array = np.zeros((N_trials,))
state = np.zeros((len(phix1_array),))
```

[6]:
```
for i in range(0,N_trials): #number of iteration for work
    ## create an array of standard gaussian distributed random numbers for␣
 ↪noise term
    randnumber = np.random.randn(len(phix1_array))
    # Determining change in phi from thermal equilibrium condition 1/2 k_BT = 1/
 ↪2 C (Phi_dot)**2
    Initial_velocity =  (2*pi/flux_quantum)*np.sqrt(k_B*T/(C*Omega_p0**2))
    dphi = Initial_velocity*dtau   #dphi calculated from thermal condition
    #initial values of the position of the particle in the potential
    phi[0] = phi_L
    phi[1] = phi[0]+ dphi
    count = 1
    #print("i", i)

    #loop to find position of the particle till the feedback point
    while  count< feedback_point:   #len(phix1_array)-1:
        phi[count+1] =␣
 ↪C1*phix0_array[count]+C2*phi[count]+C3*phi[count-1]-C4*np.
 ↪sin(phi[count])+C5*randnumber[count]
        count = count + 1

#plt.figure(4)
#plt.plot(phi)

    ##convert position to state
    for ii in range(0,feedback_point+1):
        if phi[ii]>phi_saddle:
            state[ii]=1
        else:
            state[ii] = -1

 ##Feedback process has two fast ramp
    if state[feedback_point]==1:
        while phix1_array[count]< phix1_array[-1]:
            phi[count+1] =␣
 ↪C1*phix0_array[count]+C2*phi[count]+C3*phi[count-1]-C4*np.
 ↪sin(phi[count])+C5*randnumber[count]
```

```
            count = count + 1
            state[count]=1
    else:
        while phix0_array[count]> phix0_array[-1]:
            phi[count+1] =␣
↪C1*phix0_array[count]+C2*phi[count]+C3*phi[count-1]-C4*np.
↪sin(phi[count])+C5*randnumber[count]
            count = count + 1
            state[count]= -1

    ## Select energy bias accordig the feedback point
    if state[feedback_point]==1:
        Epsilon_choosen = Epsilon1_array
    else:
        Epsilon_choosen = Epsilon0_array

## calculate heat and work
    dizWork = np.zeros((len(phix1_array),))
    Qheat = np.zeros((len(phix1_array),))
    for k in range(0,len(state)-1):
        if state[k+1]== state[k]:
            dizWork[k+1]= dizWork[k]+ 0.
↪5*state[k+1]*(Epsilon_choosen[k+1]-Epsilon_choosen[k])
            Qheat[k+1]= Qheat[k]
        else:
            dizWork[k+1]= dizWork[k]
            Qheat[k+1]= Qheat[k] - 0.5*( state[k+1]-state[k] )*(␣
↪Epsilon_choosen[k+1]+Epsilon_choosen[k] )*0.5


    Work_array[i] = dizWork[-1]
    Heat_array[i] = Qheat[-1]
print('The accumulative workdone and heat absorbed in a cycle is W={} and Q={}'.
↪format(dizWork[-1], Qheat[-1]))
```

```
The accumulative workdone and heat absorbed in a cycle is W=0.9686693885037513
and Q=0.9686693885037505
```

[7]:
```
##
fig, ax = plt.subplots(nrows=1, ncols=2, sharey=False,figsize=(12,5))
# plots
ax[0].plot(realtime_array,phi,color="blue", linewidth=1.0, linestyle="-")
ax[1].plot(realtime_array,state,color="red", linewidth=1.0, linestyle="-")
# labels
ax[0].set_ylabel(r'$\varphi$',fontsize=20)
ax[0].set_xlabel('time (ns)',fontsize=20)
ax[1].set_ylabel('state',fontsize=20)
```

```
ax[1].set_xlabel('time (ns)',fontsize=20)
# adjust right subfigure axes location
ax[1].yaxis.tick_right()
ax[1].yaxis.set_label_position("right")
# figure settings
fig.suptitle('Position of a fictitious phase particle in a cycle', fontsize=18)
fig.tight_layout()
fig.subplots_adjust(top=0.9) # tight_layout ignores overall titles (current bug)
```

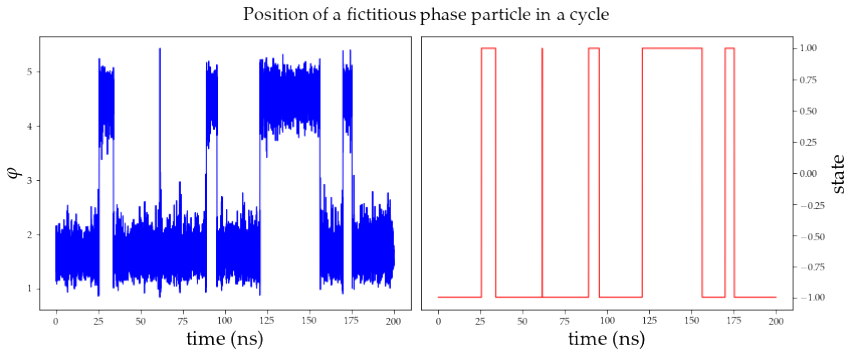

[8]:
```
##

fig, ax = plt.subplots(nrows=1, ncols=2, sharey=False,figsize=(11,5))
# plots
ax[0].plot(realtime_array,dizWork,color="blue", linewidth=1.0, linestyle="-")
ax[1].plot(realtime_array,Qheat,color="red", linewidth=1.0, linestyle="-")
# labels
ax[0].set_ylabel('$W/k_{B}T$',fontsize=18)
ax[0].set_xlabel('time(ns)',fontsize=18)
ax[1].set_ylabel('$Q/k_{B}T$',fontsize=18)
ax[1].set_xlabel('time(ns)',fontsize=18)
# adjust right subfigure axes location
ax[1].yaxis.tick_right()
ax[1].yaxis.set_label_position("right")
# figure settings
fig.suptitle('Workdone and Heat absorbed by the engine in a cycle', fontsize=18)
fig.tight_layout()
fig.subplots_adjust(top=0.9) # tight_layout ignores overall titles (current bug)
```

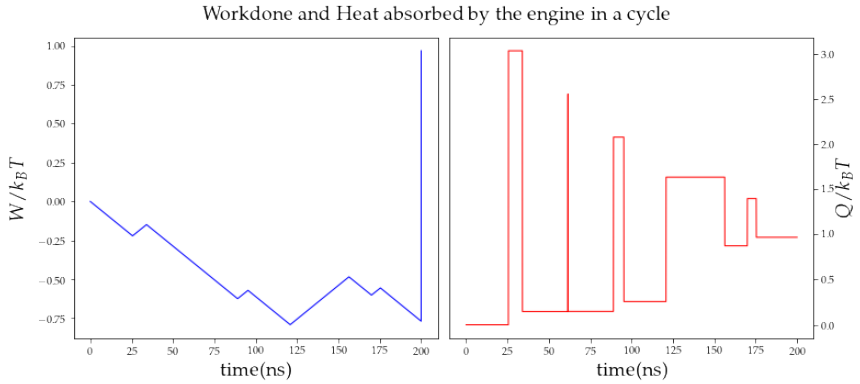

[9]:
```
"""Created on Fri Jul 13 18:19:18 2018 @author: Suman Dhamala
This code is to compute the escape rate from one of the well of
the 1D flux logic device using Monte-carlo method. The simulation
can be performed for different barrier height of the potential
controlled by beta_L and for different tilt controlled by
phi_x. The simulation can be run for different T and potential
configurations."""

# Variables
N_jumps = 5  # no. of ineration for a particular T.
T = [4.2]  # Temperature in the unit of K
phix = 0.5*2*pi # phi_x for symmetric potential

## initializ
norm_time_left = np.zeros((N_jumps, len(T)) )


for ii in range(len(T)):
# Determining change in phi from thermal equilibrium condition 1/2 k_BT = 1/2 C␣
 ↪(Phi_dot)**2
    Initial_velocity =  (2*pi/flux_quantum)*np.sqrt(k_B*T[ii]/(C*Omega_p0**2))
    dphi = Initial_velocity*dtau   #dphi calculated from thermal condition
    C5 = np.sqrt(2*G*k_B*T[ii]*dtau3/E_J) # C5 is the coefficient of the noise␣
 ↪term

    for jump in range(0,N_jumps):
        randnumber = np.random.randn()
        # Initial position
        phi1 = phi_L
        phi2 = phi1 + (-1)**jump*dphi
```

```
        count=0
        phi3 = C1*phix + C2*phi2 + C3*phi1 - C4*np.sin(phi2) + C5*randnumber
        phi1 = phi2; # order matters
        phi2 = phi3;

        while phi2 < phi_saddle:
            randnumber = np.random.randn()
            count = count+1;
            phi3 = C1*phix + C2*phi2 + C3*phi1 - C4*np.sin(phi2) + C5*randnumber
            phi1 = phi2  # order matters
            phi2 = phi3

        ##
        norm_time_left[jump,ii] = count*dtau

tau_aver_left = np.mean(norm_time_left)
Rate_left = (1/tau_aver_left)*Omega_p0
print('The transition rate for G={} is {}/s'.format(G, Rate_left))
```

```
The transition rate for G=0.1 is 139143165.47785825/s
```